iScience

CellPress
OPEN ACCESS

Article

EMT alterations in the solute carrier landscape uncover SLC22A10/A15 imposed vulnerabilities in pancreatic cancer

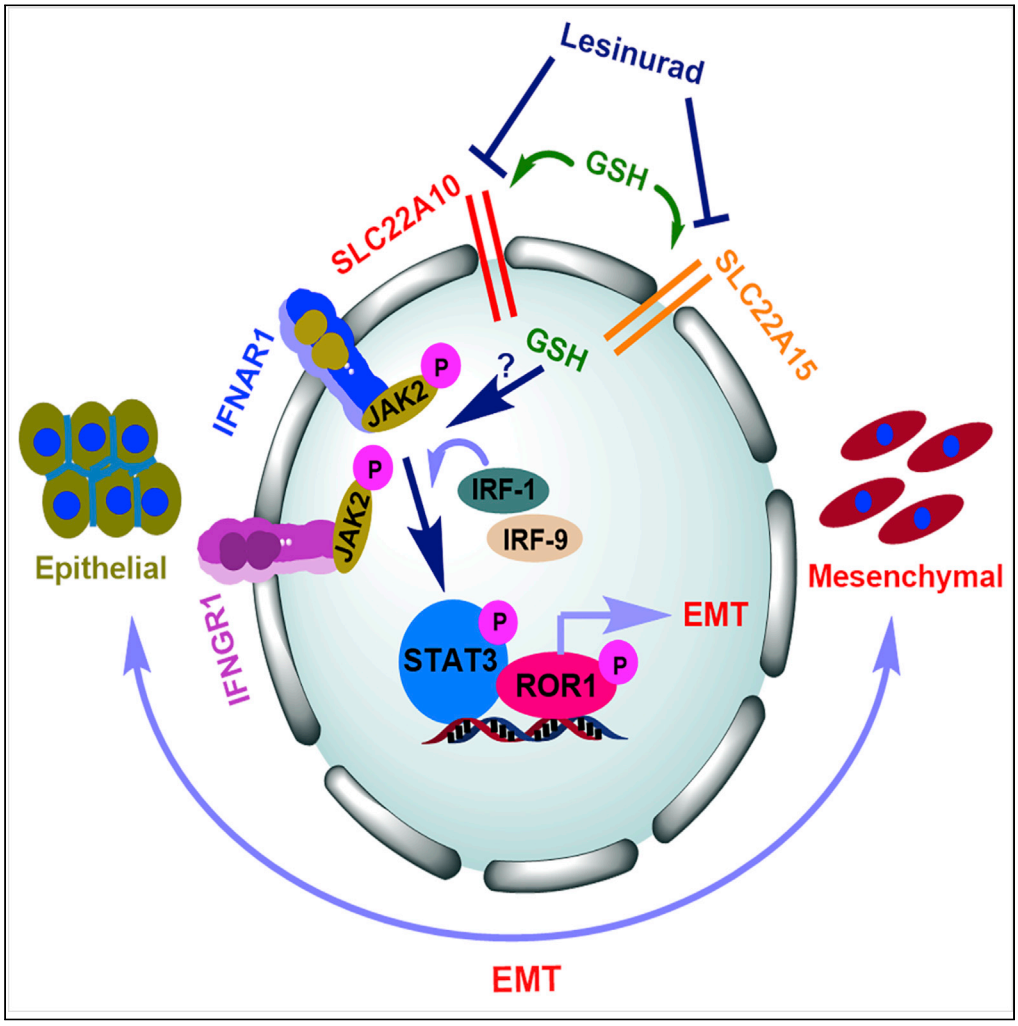

Debasis Nayak, Brenna Weadick, Avinash K. Persaud, ..., Junan Li, Moray J. Campbell, Rajgopal Govindarajan

govindarajan.21@osu.edu

Highlights

Comprehensive transportome analysis identifies key SLC alterations during PDAC EMT

SLC22A10 and SLC22A15 trigger IFN signaling to promote PDAC aggressiveness

SLC22A10 and SLC22A15 facilitate glutathione accumulation to promote IFN signaling

Lesinurad impeded the SLC22A10/15 adverse effects in PDAC mouse models

Nayak et al., iScience *25*, 104193
May 20, 2022
https://doi.org/10.1016/j.isci.2022.104193

iScience

CellPress
OPEN ACCESS

Article

EMT alterations in the solute carrier landscape uncover SLC22A10/A15 imposed vulnerabilities in pancreatic cancer

Debasis Nayak,[1] Brenna Weadick,[1] Avinash K. Persaud,[1] Radhika Raj,[1] Reena Shakya,[2] Junan Li,[3] Moray J. Campbell,[4,5] and Rajgopal Govindarajan[1,6,7,*]

SUMMARY

The involvement of membrane-bound solute carriers (SLCs) in neoplastic transdifferentiation processes is poorly defined. Here, we examined changes in the SLC landscape during epithelial-mesenchymal transition (EMT) of pancreatic cancer cells. We show that two SLCs from the organic anion/cation transporter family, SLC22A10 and SLC22A15, favor EMT via interferon (IFN) α and γ signaling activation of receptor tyrosine kinase-like orphan receptor 1 (ROR1) expression. In addition, SLC22A10 and SLC22A15 allow tumor cell accumulation of glutathione to support EMT via the IFNα/γ-ROR1 axis. Moreover, a pan-SLC22A inhibitor lesinurad reduces EMT-induced metastasis and gemcitabine chemoresistance to prolong survival in mouse models of pancreatic cancer, thus identifying new vulnerabilities for human PDAC.

INTRODUCTION

Pancreatic ductal adenocarcinoma (PDAC), which is considered a lethal malignancy because of its extremely low patient survival rate, is projected to become the second leading cause of cancer-related patient mortality (Neoptolemos et al., 2018). High PDAC patient mortality is largely attributed to the rapid nature of PDAC metastasis and the lack of efficacious treatment options. Epithelial-mesenchymal transition (EMT) is a neoplastic transdifferentiation program that is implicated in local tissue metastasis, early systemic dissemination, and chemoresistance in pancreatic cancer (Aiello et al., 2017; Arumugam et al., 2009; Rhim et al., 2012). Many genetic and epigenetic changes drive EMT, causing the transformation of indolent epithelial cells into more migratory and invasive mesenchymal cells. For example, the loss of epithelial cell adhesion molecule E-cadherin and/or the acquisition of another neuronal (N)-cadherin, termed as cadherin switching, facilitates the exit of tumor cells from the primary tumor niche and their invasion and metastasis (Lamouille et al., 2014). Further, the metabolic requirements of aggressive cancer cells change dramatically, and metabolic pathways are rewired to support the invasion and migration of cancer cells (Bott et al., 2019; Elia et al., 2018; Hu et al., 2021). Moreover, metastasizing cancer cells experience stress during circulation; thus, these cells are highly reliant on an antioxidant metabolism to scavenge reactive oxygen species and combat oxidative stress (Piskounova et al., 2015). Furthermore, the premetastatic niche is programmed for glucose metabolism (Fong et al., 2015). In addition, metastatic colonization at a distant site requires ATP production to fuel the increasing nutritional needs of metastasized cells (Elia et al., 2017; Loo et al., 2015). Given the intricate, yet distinctive, events of EMT in pancreatic cancer, it is vital to identify crucial players orchestrating these deleterious effects, which may help identify new strategies to reduce metastasis and chemoresistance and improve treatment outcomes for pancreatic cancer patients.

The SLC superfamily, which contains nearly 400 SLCs, is the second largest group of membrane proteins in the human genome (subsequent to G protein-coupled receptors), yet they are largely understudied in cancer (Höglund et al., 2011; Panda et al., 2020; Schaller and Lauschke, 2019). It is likely that SLCs support the requirements of cancer cells to not only maintain biosynthetic supply but also adjust to the changing demands of cancer cells, such as those occurring in the multistep metastatic cascade and the acquisition of chemoresistance (El-Gebali et al., 2013; Sutherland et al., 2020; Wang and Zou, 2020). The protumorigenic roles of SLCs also render them important druggable targets for cancer therapy, as blocking or activating their expression could potentially restrain tumor progression (Garibsingh and Schlessinger, 2019;

[1]Division of Pharmaceutics and Pharmacology, The Ohio State University College of Pharmacy, Columbus, OH 43210, USA

[2]Target Validation Shared Resource, The Ohio State University Comprehensive Cancer Center, Columbus, OH 43210, USA

[3]The Ohio State University College of Pharmacy, Columbus, OH 43210, USA

[4]Molecular Carcinogenesis and Chemoprevention Program, The Ohio State University Comprehensive Cancer Center, Columbus, OH 43210, USA

[5]Biomedical Informatics Shared Resource, The Ohio State University, Columbus, OH 43210, USA

[6]Translational Therapeutics, The Ohio State University Comprehensive Cancer Center, Columbus, OH 43210, USA

[7]Lead contact

*Correspondence: govindarajan.21@osu.edu

https://doi.org/10.1016/j.isci.2022.104193

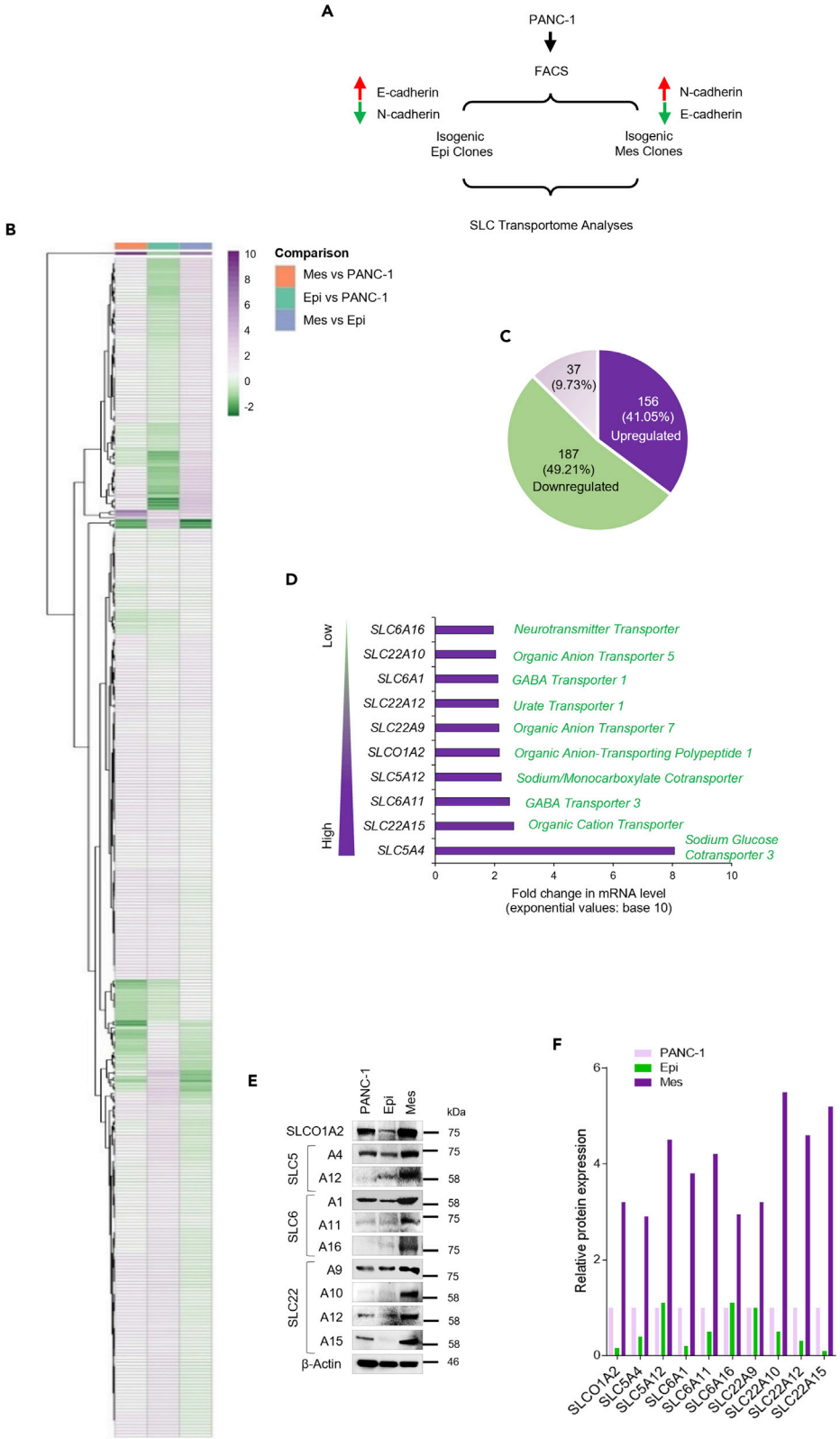
A
PANC-1
FACS
E-cadherin
N-cadherin
N-cadherin
E-cadherin
Isogenic
Epi Clones
Isogenic
Mes Clones
SLC Transportome Analyses
B
Comparison
Mes vs PANC-1
Epi vs PANC-1
Mes vs Epi
10
8
6
4
2
0
-2
C
37
(9.73%)
156
(41.05%)
Upregulated
187
(49.21%)
Downregulated
D
Low
High
SLC6A16
Neurotransmitter Transporter
SLC22A10
Organic Anion Transporter 5
SLC6A1
GABA Transporter 1
SLC22A12
Urate Transporter 1
SLC22A9
Organic Anion Transporter 7
SLCO1A2
Organic Anion-Transporting Polypeptide 1
SLC5A12
Sodium/Monocarboxylate Cotransporter
SLC6A11
GABA Transporter 3
SLC22A15
Organic Cation Transporter
SLC5A4
Sodium Glucose
Cotransporter 3
0
2
4
6
8
10
Fold change in mRNA level
(exponential values: base 10)
E
PANC-1
Epi
Mes
kDa
SLCO1A2
SLC5
A4
A12
SLC6
A1
A11
A16
SLC22
A9
A10
A12
A15
β-Actin
75
75
58
58
75
75
58
58
58
46
F
PANC-1
Epi
Mes
Relative protein expression
6
4
2
0
SLCO1A2
SLC5A4
SLC5A12
SLC6A1
SLC6A11
SLC6A16
SLC22A9
SLC22A10
SLC22A12
SLC22A15

Figure 1. Alterations in SLC transporters during EMT in pancreatic cancer

(A) Isolation of the Epi and Mes clones from parental PANC-1 (human PDAC cell line) utilized for transcript analyses of the SLC transportome.

(B) Heatmap depicting alterations in the mRNA levels of 380 SLC transporter genes determined by real-time qPCR analysis. The differentially expressed genes between Mes clones versus PANC-1 cells, Epi clones versus PANC-1 cells and Mes clones versus Epi clones are presented in separate columns. The color gradient from green to purple indicates log2-transformed fold-change values from −2 to 10.

(C) Pie chart analysis showing the distribution of 380 SLCs based on their mRNA levels in Mes clones compared with Epi clones. Fold-change values: >1.2, upregulated; 0.8–1.2, unchanged; <0.8, downregulated.

(D) The top 10 SLC genes whose mRNA levels are altered by a > 800-fold in Mes clones compared with Epi clones. Fold increases in mRNA levels are presented as exponential values (base of 10).

(E) Western blots showing endogenous protein expression of the EMT-induced SLCs in PANC-1 cells and the Epi and Mes clones. Western blots represent three independent experiments. β-Actin was used as an endogenous loading control.

(F) Densitometry analysis of the Western blots presented in (E) showing the relative protein expression of SLCs in PANC-1 cells and Epi and Mes clones.

Lin et al., 2015). Recent studies are beginning to uncover the involvement of specific SLCs in cancer survival, disease progression, and drug resistance (Parker et al., 2020; Payen et al., 2017; Van Geldermalsen et al., 2016); however, a comprehensive understanding of changes in SLCs during the PDAC EMT process has not been developed. In an attempt to expose SLC imposed vulnerabilities in EMT as an approach to inhibit metastasis and reduce chemoresistance in PDAC (César-Razquin et al., 2015), here we investigated the alterations in SLC transportome using an EMT model of pancreatic cancer. Using molecular, genetic, and pharmacological approaches, we uncovered the SLC22A10 and SLC22A15 transporters to favor PDAC EMT, identified the activation of interferon-α/γ-driven ROR1 signaling by SLC22A10 and SLC22A15, and proposed a novel combinational therapeutic approach for the attenuation of EMT-associated metastasis and drug resistance in pancreatic cancer.

RESULTS

SLC22A10 and SLC22A15 promote EMT of pancreatic cancer

To examine the SLC landscape transition between neoplastic epithelia and mesenchyme, we utilized a cadherin-switching model of EMT in pancreatic cancer. This model comprises of isogenic epithelial (E-cadherin enriched, N-cadherin depleted) and mesenchymal (N-cadherin enriched, E-cadherin depleted) subclones of pancreatic cancer cells derived from human PANC-1 cell line (Figure 1A). We earlier reported PANC-1 mesenchymal sublines are aggressive in nature, highly metastatic, and less responsive to chemotherapy than that of an epithelial subtype (Weadick et al., 2021). An SLC-specific microfluidic array quantitative real-time PCR analysis of ∼380 SLCs (>90% SLC coverage) showed the differentially expressed genes (DEGs) based on transcript levels in either epithelial (Epi) or mesenchymal (Mes) clones versus parental PANC-1 cells and the Mes clones versus Epi clones with 18S ribosomal RNA used as an internal control (Table S1 and Figure 1B). The data revealed that 41.05% (156 out of 380) of SLCs were upregulated (fold change >1.2), 49.21% (187 out of 380) were downregulated (fold change ≤0.8), and 9.73% (37 out of 380) remained unchanged (fold change of 0.8–1.2) in the Mes clones compared with the Epi clones (Figure 1C), suggesting the reprogramming of SLCs during EMT.

To investigate whether highly upregulated SLCs contribute to the aggressiveness of the Mes clone, we examined the SLCs most upregulated in the Mes clones compared with the Epi clones. The top upregulated SLCs (fold change >800) include SLC5A4, SLC22A15, SLC6A11, SLC5A12, SLCO1A2, SLC22A9, SLC22A12, SLC6A1, SLC22A10, and SLC6A16 (Figures S1A and S1D). Although SLCs mRNAs and proteins generally do not correlate well, the endogenous protein expression of all 10 SLCs was much higher in the Mes clone, in contrast to their basal expression in PANC-1 cells and diminished expression in the Epi clones (Figures 1E and 1F). To determine the ability of highly upregulated SLCs in Mes clone to promote pancreatic tumor growth and metastasis, we developed clones stably overexpressing (OE) these SLCs from parental PANC-1 cells through lentiviral transduction (equal multiplicity of infection) and subsequent puromycin selection (Figure S1B). Interestingly, cells overexpressing four SLCs belonging to the organic anion/cation SLC22 gene family (SLC22A9, SLC22A10, SLC22A12, and SLC22A15) exhibited relatively more spindle-shaped morphologies with a reduced expression of epithelial keratins cytokeratin 8 and 18 at the mRNA level (Figures 2A and 2B). In addition, these four SLC OE cells demonstrated a reduced expression of other epithelial protein markers (E-cadherin, ZO-1, and Occludin), increased expression of mesenchymal protein markers (N-cadherin, ZEB1, SLUG, Vimentin, and TWIST1), and increased migration

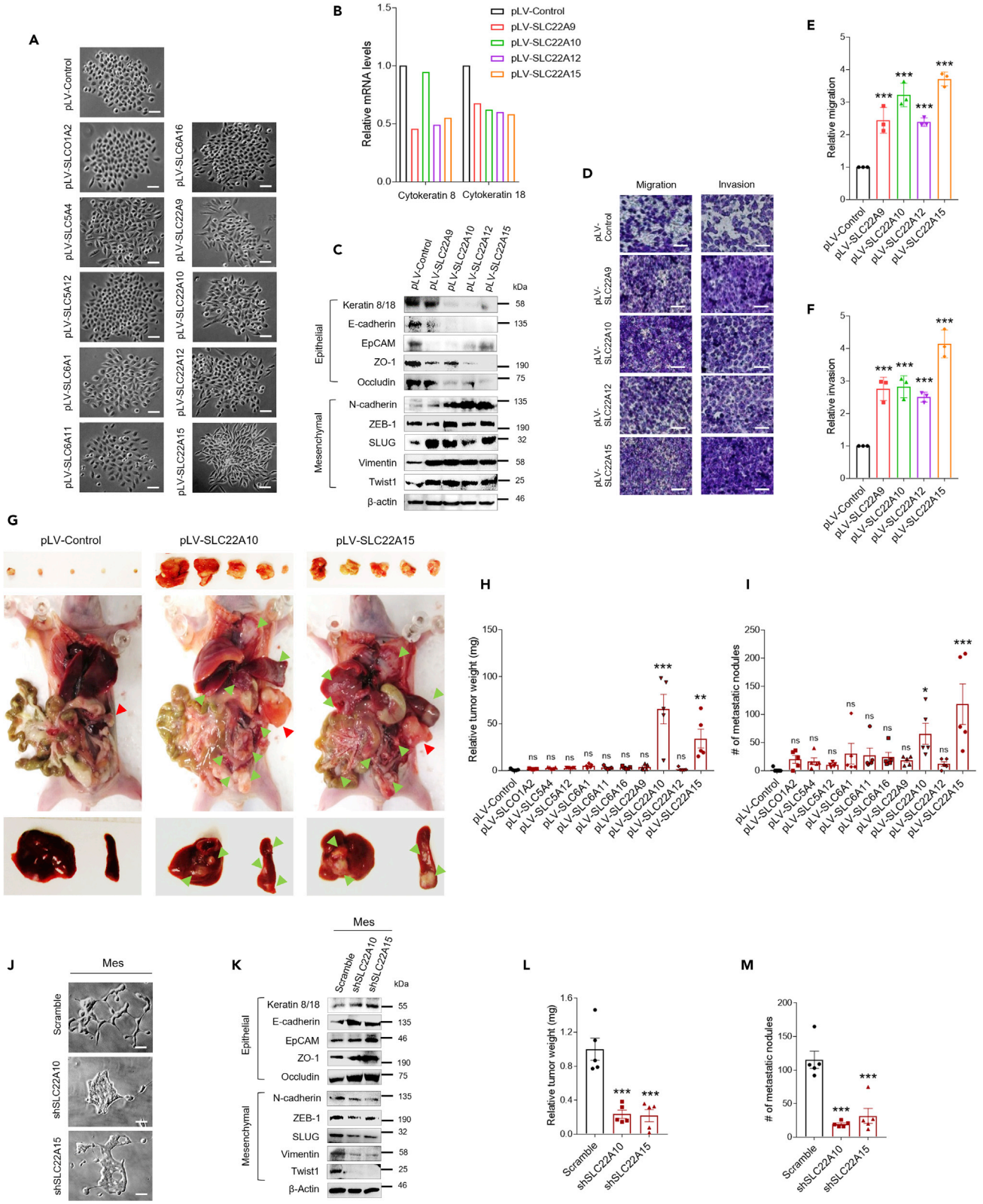
A
pLV-Control
pLV-SLCO1A2
pLV-SLC5A4
pLV-SLC5A12
pLV-SLC6A1
pLV-SLC6A11
pLV-SLC6A16
pLV-SLC22A9
pLV-SLC22A10
pLV-SLC22A12
pLV-SLC22A15
B
Relative mRNA levels
Cytokeratin 8
Cytokeratin 18
pLV-Control
pLV-SLC22A9
pLV-SLC22A10
pLV-SLC22A12
pLV-SLC22A15
C
kDa
Epithelial
Keratin 8/18
E-cadherin
EpCAM
ZO-1
Occludin
Mesenchymal
N-cadherin
ZEB-1
SLUG
Vimentin
Twist1
β-actin
D
Migration
Invasion
E
Relative migration
F
Relative invasion
G
pLV-Control
pLV-SLC22A10
pLV-SLC22A15
H
Relative tumor weight (mg)
I
# of metastatic nodules
J
Mes
Scramble
shSLC22A10
shSLC22A15
K
Mes
Scramble
shSLC22A10
shSLC22A15
L
Relative tumor weight (mg)
M
# of metastatic nodules

Figure 2. Identification of SLC22A10 and SLC22A15 as promoters of EMT and metastasis in pancreatic cancer

(A) Representative phase contrast images of the stable clones transduced with vector and overexpressing the SLCs showing their morphological features and cell scattering. Scale bars, 50 μm $n = 5$ random fields were photographed and analyzed from each condition.

(B) Relative mRNA levels of epithelial markers Cytokeratin 8 and Cytokeratin 18 in SLC22-OE clones determined by RNA sequencing of these clones and subsequent DE analysis of the genes.

(C) Western blotting analyses of whole-cell lysates from SLC22-OE clones showing the protein expression of epithelial and mesenchymal markers. β-Actin was used as an endogenous loading control. Data represent three independent experiments.

(D) Representative crystal violet-stained images of migrated and invaded SLC22-OE clones. Scale bars, 50 μm $n = 5$ random fields from each condition were photographed and analyzed.

(E and F) Quantification of the number of migrated and invaded SLC22-OE clones depicted in fold-change values relative to the control clone. Error bars, mean ± SD.

(G) Representative necropsy images of mice harboring tumors from vector-transduced and SLC22A10- and SLC22A15-OE clones showing the primary tumors (red arrows) and secondary tumors (green arrows) (middle panel). Images of dissected primary tumors (upper panel) and metastatic foci in the liver and spleen (lower panel) are shown separately. Arrows point at tumors, metastatic foci, or related lesions. $n = 5$ mice per group.

(H) Quantification of the weights of primary tumors dissected from groups of animals harboring SLC clones at the end of the experiment. Error bars, mean ± SEM. $n = 5$ mice per group; each point represents one animal.

(I) Quantification of the average number of metastatic foci in the vital organs and the abdominal cavities of animals in each group in the study. Error bars, mean ± SEM. $n = 5$ mice per group; each point represents one animal.

(J) Representative phase contrast images of scramble-, shSLC22A10-, and shSLC22A15-transduced clones. Scale bars, 50 μm $n = 5$ random fields photographed and analyzed from each condition.

(K) Western blotting analyses of whole cell lysates showing the protein expression of epithelial and mesenchymal markers in scramble-, shSLC22A10-, and shSLC22A15-transduced clones. β-Actin was used as an endogenous loading control for the Western blots. Data represent three independent experiments.

(L) Quantification of the weights of primary tumors dissected from mice harboring tumors from scramble-, shSLC22A10-, and shSLC22A15-transduced clones. Error bars, mean ± SEM. $n = 5$ mice per group; each point represents one animal.

(M) Quantification of the average number of metastatic foci in the abdominal viscera of animals in each group in the study. Error bars, mean ± SEM. $n = 5$ mice per group; each point represents total number of metastatic nodules from one animal. Data presented in (E, F, H, I, L, and M) were analyzed by one-way ANOVA with Dunnett's multiple comparisons test. $^{*}p < 0.05$; $^{**}p < 0.01$; $^{***}p < 0.001$; ns, not significant.

and invasiveness (Figures 2C–2F). Because SLC22A transporters conduct membrane translocation of a diverse range of organic solutes (anionic, cationic, and zwitterionic) that can support EMT, we further examined the effects of these SLCs on tumor development by orthotopically implanting SLC OE cells into athymic mouse pancreases (Figure S1B). Interestingly, mice harboring tumors SLC22A10- and SLC22A15-OE clones had significantly enlarged tumors compared with those of mice harboring the vector-transduced clone. In addition, a dramatic increase in metastatic nodules over the abdominal organs including liver and spleen was noticeable in mice-bearing tumors from both SLC22A10- and SLC22A15-OE clones (Figures 2G–2I). Comparatively, mice-bearing tumors from the SLC22A15-expressing clone had a smaller tumor size at the injection site compared with those bearing tumors from the SLC22A10-expressing clone; however, the extent and number of metastatic nodules were much higher in the SLC22A15 group. The remaining six SLC-expressing clones, including SLC22A9 and SLC22A12, produced modest, non-significant increases, or no changes in tumor volumes and metastatic tumor burden. Noticeably, SLC22A10 OE clones also induced the protein expression of SLC22A15 in PANC-1 (Figure S1C). In contrast, neither of the two SLCs was able to induce the expression of other known oncogenic SLCs such as SLC1A5, SLC6A6, and SLC16A1 in PANC-1 at the transcript level (Figure S1D). The effect of SLC22A10 and SLC22A15 on EMT was also observed in HPAF-II, which showed the reduced E-cadherin and augmented N-cadherin, Twist1, and SLUG expression upon OE of these SLCs (Figures S1C and S1E).

To test the observed phenotypes with SLC22A10 and SLC22A15 are not owing to overexpression artifacts, we next conducted genetic silencing experiments and studied whether the loss of SLC22A10 and SLC22A15 could suppress pancreatic tumor growth and metastasis in aggressive Mes clones. Short hairpin RNAs for SLC22A10 and SLC22A15 were introduced in Mes clones using lentiviral transductions to produce stable knockdowns. The shSLC22A10- and shSLC22A15-introduced knockdown Mes clones (clone #C in both) showed a reduced expression of respective proteins with increased epithelial morphology, increased cell-cell adhesion, and reduced cell scattering compared with the scramble-transduced Mes clone (Figures S1F and S2J). Furthermore, the protein levels of epithelial markers (Keratin 8/18, E-cadherin, ZO-1, and Occludin) were restored, and the expression of mesenchymal markers (N-cadherin, ZEB-1, SLUG, Vimentin, and Twist-1) was downregulated in the shSLC22A10- and shSLC22A15-transduced Mes clones (Figure 2K). Moreover, orthotopic injection of the shSLC22A10- and shSLC22A15-transduced Mes clones into the pancreas of athymic nude mice restricted tumor growth and reduced the metastatic spread of cancer cells to abdominal viscera when compared with GIPZ-shRNA-transduced Mes clone (Figures S1G,

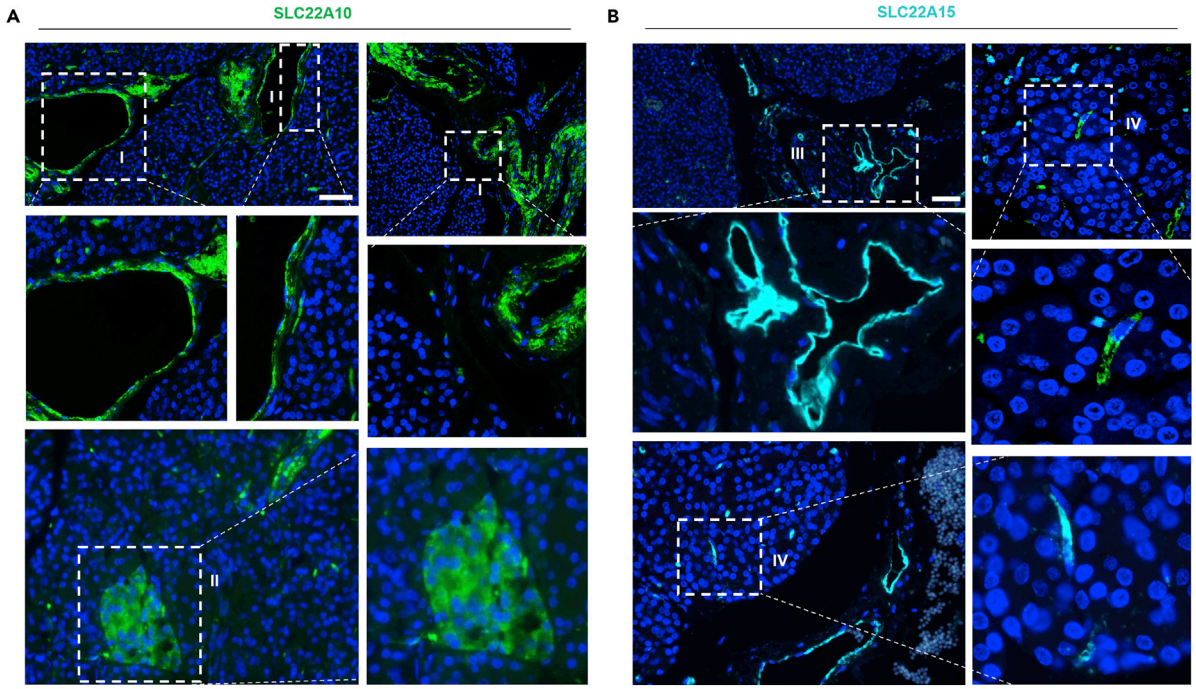

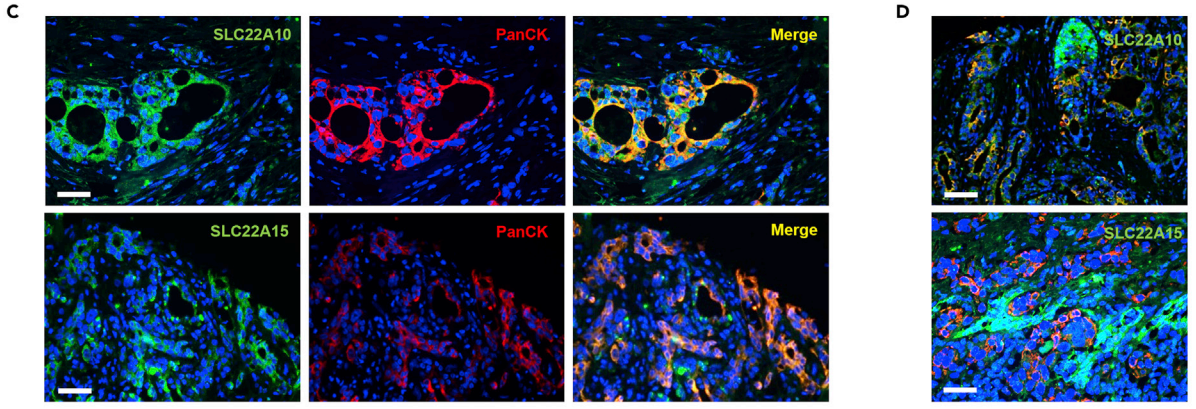

E

	Normal	Tumor	P value*
SLC22A10 H scores			
Mean (sd)	6.5 (6.0)	44.1 (51.7)	<0.001[a]
Mean (range)	3.9 (2.1, 16.6)	26 (9.3, 59.8)	0.007[b]
Sample size	5	86	
Frequency		Higher: 81.4% Lower: 18.6%	
SLC22A15 H scores			
Mean (sd)	5.7 (3.0)	37.6 (37.2)	<0.001[a]
Mean (range)	5.2 (2.5, 9.3)	24 (10.5, 47)	0.006[b]
Sample size	5	91	
Frequency		Higher: 87.9% Lower: 12.1%	

F

H Score	SLC22A10	SLC22A15	P value*
Tumor			
Mean	48.8	49.7	0.50
Sample size	86	91	
Stroma			
Mean	6.2	18.9	<0.0001
Sample size	86	91	

G

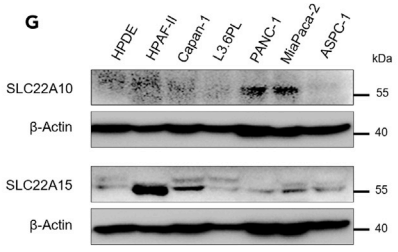

Figure 3. Increased expression of SLC22A10 and SLC22A15 in human pancreatic cancers

(A) Representative images of IHC staining in human normal pancreatic tissues showing the expression of SLC22A10 (green) in ductal epithelial cells (I) and pancreatic islet cells (II). Insets display the enlarged view of boxed regions. Nuclei stained with DAPI are blue. Scale bars, 50 μm $n = 3$ samples per condition.

(B) Representative images of IHC staining in human normal pancreatic tissues showing the expression of SLC22A15 (cyan) in ductal epithelial cells (III) and pancreatic stellate cells surrounding the acini (IV). Insets display the enlarged view of boxed regions. Nuclei stained with DAPI are blue. Scale bars, 50 μm $n = 3$ samples per condition.

(C) Representative images of IHC staining in human pancreatic cancer tissues showing expression of SLC22A10 or SLC22A15 (green), Pan Cytokeratin (PanCK) (red), and their colocalization (yellow). Nuclei stained with DAPI are blue. Scale bars, 50 μm.

(D) Representative images of multiplexed IHC staining in human pancreatic cancer tissue microarray (TMA) illustrating the predominant expression of SLC22A10 in tumor (Pan-CK positive; yellow) and SLC22A15 in stromal (Pan-CK negative; green) regions, respectively. Nuclei stained with DAPI are blue. Scale bars, 50 μm.

(E) H-scores of SLC22A10 and SLC22A15 in human normal pancreatic tissues and human pancreatic cancer TMA as determined by quantification of the IHC images using inForm software. The intensity and frequency of expression of these two SLCs in human pancreatic tumor tissues in comparison with human normal pancreatic tissues are presented. For the data presented in C-F, $n = 86–91$ patient-derived pancreatic cancer tissue samples were analyzed.

(F) Histoscores (H-scores) of SLC22A10 and SLC22A15 expression intensity in human pancreatic tumor and stromal compartments from quantitative IHC multiplexing of human pancreatic cancer TMA. Data presented in (E and F) were analyzed by two-sided [a]Student's *t*-test and [b]U rank sum test with level of significance 0.05.

(G) Western blots depicting the expression of SLC22A10 and SLC22A15 in normal human pancreatic ductal epithelial (HPDE), and a panel of six human PDAC cell lines (HPAF-II, Capan-1, L3.6PL, PANC-1, MiaPaca-2, and AsPC-1). β-Actin was used as a loading control. Data represent three independent experiments.

S1H, S2L, and S2M). Taken together, these results suggested the specific roles of SLC22A10 and SLC22A15 in driving EMT phenotypes of pancreatic cancer cells.

To evaluate the clinical relevance of SLC22A10 and SLC22A15 in humans with pancreatic cancers, we characterized the expression of SLC22A10 and SLC22A15 in normal pancreatic tissues, pancreatic cancerous tissues, and pancreatic cancer cell lines. The expression of SLC22A10 and SLC22A15 has not been studied in humans before; therefore, antibodies against SLC22A10 and SLC22A15 were tested on several normal human tissues using immunohistochemical analysis prior to examination of pancreatic cells and tissues. As expected of many SLC22 transporters, both SLC22A10 and SLC22A15 were found to be well expressed in kidney tubular epithelial cells. Interestingly, the expression of SLC22A10 and SLC22A15 was observed in distinct renal tubular segments (SLC22A10 in collecting ducts and SLC22A15 in distal tubules), indicating specificity of these antibodies to the respective proteins (Figures S2A and S2B). When we analyzed SLC22A10 and SLC22A15 expression in normal human pancreatic tissues, we detected SLC22A10 protein in the epithelial cells lining the large intralobular and interlobular ducts with predominant localization at the cell surface. In addition, an intense expression of SLC22A10 protein was observed in the islets of Langerhans. On the other hand, the SLC22A15 expression was predominantly detected in the large intralobular and interlobular ducts and distinctly elongated stellate cells surrounding the normal pancreatic acini, with no expression in the islets of Langerhans (Figures 3A and 3B).

To determine the expression of SLC22A10 and SLC22A15 in human pancreas cancers, we examined patient-derived pancreatic cancer tissues ($n = 86$) via a tumor microarray (TMA; Table S2) using multiplexed immunohistochemical analyses. The expression of SLC22A10 and SLC22A15 was quantified in the tumor (pan-cytokeratin positive) and stromal (pan-cytokeratin negative) cells (Figures 3C and 3D) based on the fluorescent signal intensity to produce an H (histo)-score ranging from 0 to 300 for each image (see STAR Methods). When the SLC22A10 and SLC22A15 intensity of expression was compared between the human normal and cancerous pancreatic tissues in TMA, we found a higher expression of SLC22A10 (81.4% cases; $p < 0.001$) and SLC22A15 (87.9% cases; $p < 0.001$) in cancerous tissues (Figure 3E). Interestingly, the SLC22A10 expression was identified predominantly in the tumor compartment, whereas, in the case of SLC22A15, an increased expression was distinctive in both the tumor and stromal compartments in PDAC (Figures 3D and 3F). An increased protein expression of SLC22A10 and SLC22A15 was also detected in multiple PDAC cell lines (SLC22A10 in PANC-1 and MiaPaCa-2; SLC22A15 in HPAF-II, Capan-1, and MiaPaca-2) when compared with the expression in normal human pancreatic ductal epithelial cell line HPDE (Figure 3G). Together, these findings demonstrate the putative role of increased expression of SLC22A10 and SLC22A15 in at least a subset of pancreatic tumors and cell lines supporting the EMT program of pancreatic cancer.

SLC22A10 and SLC22A15 activate ROR1 via IFN-α/γ signaling

To elucidate the molecular mechanism of action by which SLC22A10 and SLC22A15 increase the pancreatic cancer metastasis, we conducted RNA sequencing (RNA-seq) of clones stably OE vector (LV-Control),

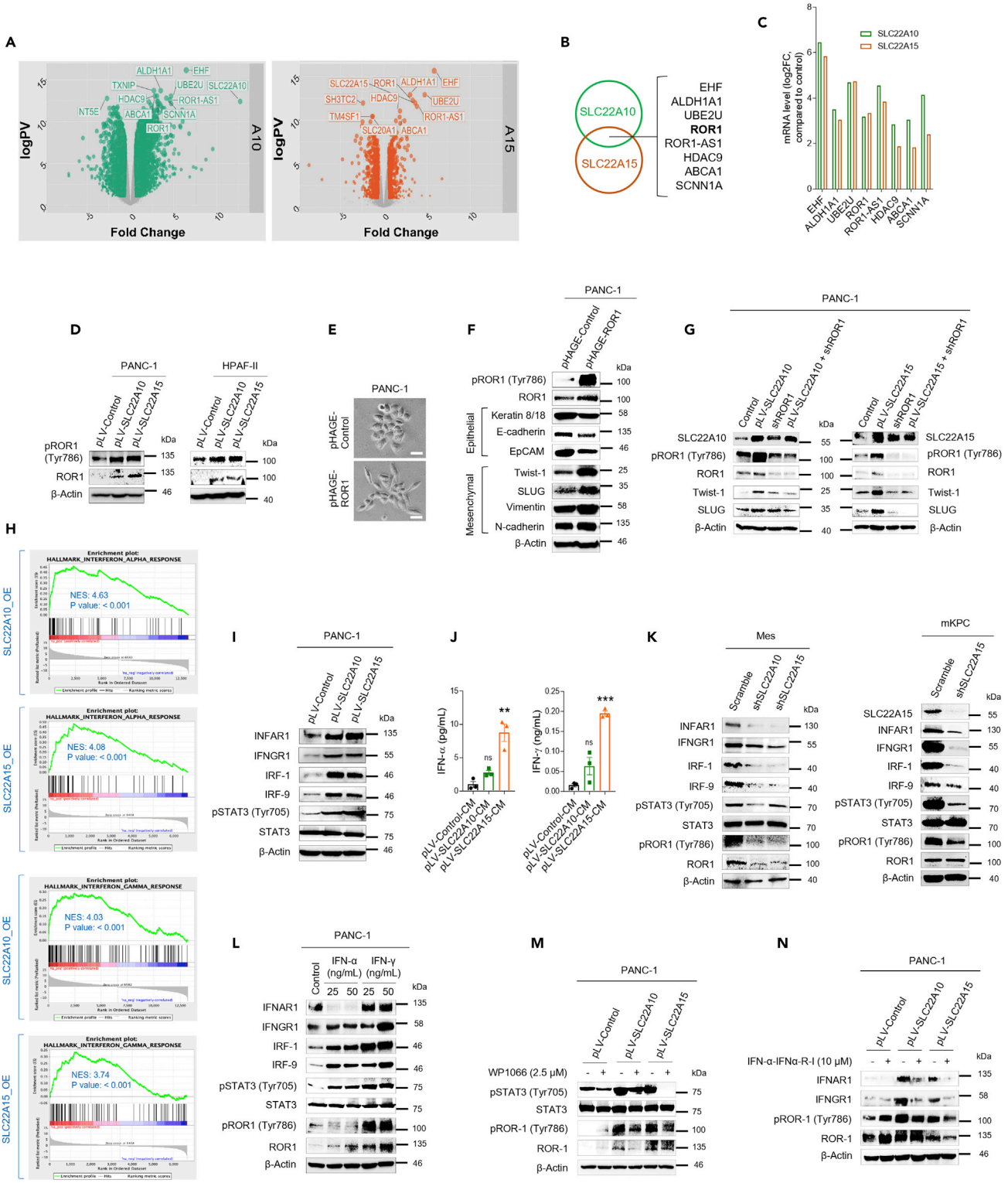

Figure 4. SLC22A10 and SLC22A15 induce ROR1 activation and EMT via IFN/STAT3 signaling pathway

(A) Volcano plots demonstrating global transcriptional changes in SLC22A10- and SLC22A15-OE clones versus vector-transduced clone as determined by RNA-seq analysis. Each circular dot indicates one gene. X axis: log2 fold change; Y axis: logP-values. Highlighted genes inside rectangles are the most significantly differentially expressed genes in cells expressing SLC22A10 (left) and SLC22A15 (right).

Figure 4. *Continued*

(B) Venn diagram showing the most significantly differentially expressed genes common to both SLC22A10- and SLC22A15-OE clones as unveiled by RNA-seq analysis.

(C) mRNA levels of top genes most significantly differentially expressed in both SLC22A10- and SLC22A15-OE clones compared with the control clone. For the data presented in (A-C), $n = 3$ independent biological replicates of each sample were used for the RNA-seq.

(D) Western blots showing protein expression of pROR1 (Tyr786), and ROR1 in control, SLC22A10-OE, and SLC22A15-OE clones in PANC-1 and HPAF-II cells. β-Actin was used as a loading control. Western blots shown represent three independent experiments.

(E) Representative phase contrast images of PANC-1 cells captured 72 h post-transduction with lentiviral particles of vector or pHAGE-ROR1. Scale bars, 50 μm $n = 3$ random fields photographed and analyzed from each condition.

(F) Western blots showing the protein expression of total and phosphorylated ROR1 and epithelial and mesenchymal markers in PANC-1 cells transduced with lentiviral particles of vector or pHAGE-ROR1. β-Actin was used as a loading control. Results represent three independent experiments.

(G) Western blots assessing the protein expression of SLC22A10, SLC22A15, pROR1 (Tyr786), ROR1, and epithelial, and mesenchymal markers in SLC22A10-OE, SLC22A15-OE, shRNA-ROR1, SLC22A10-OE + shROR1, and SLC22A15-OE + shROR1 transduced clones. β-Actin was used as a loading control. Results represent at least three independent experiments performed.

(H) GSEA enrichment plot displaying the enrichment of hallmark IFN-α and IFN-γ pathway genes in SLC22A10- and SLC22A15-OE clones. NES: enrichment score normalized to mean enrichment of random samples of the same size. $n = 3$ independent biological replicates of each RNA sample (pLV-Control, pLV-SLC22A10, and pLV-SLC22A15) were sequenced and analyzed.

(I) Western blots assessing the protein expression of key players of the IFN-α and IFN-γ signaling pathway in vector-transduced and SLC22A10- and SLC22A15-OE clones. β-Actin was used as a loading control. Data represent three independent experiments.

(J) Quantification of IFN-α and IFN-γ in the conditioned medium (CM) collected from vector-control, SLC22A10- and SLC22A15-OE clones. Error bars: mean ± SD.

(K) Western blots displaying the protein expression of key players of the IFN-α and IFN-γ signaling pathway including pROR1 (Tyr786), and ROR1 in stable clones of shRNA-Control (scramble), shSLC22A10, and shSLC22A15 developed in Mes and mKPC cells. β-Actin was used as a loading control. Western blots shown represent three independent experiments.

(L) Western blots depicting the protein expression of markers of the IFN-STAT3-ROR1 signaling axis in PANC-1 cells treated with the indicated concentrations of IFN-α and IFN-γ for 48 h β-Actin was used as a loading control. Western blots shown represent three independent experiments.

(M) Western blots assessing the protein expression of pSTAT3 (Tyr705), STAT3, pROR1 (Tyr786), and ROR1 in vector-transduced and SLC22A10- and SLC22A15-OE clones treated with WP1066 (2.5 μM) for 24 h β-Actin was used as a loading control. Western blots shown represent at least three independent experiments.

(N) Western blots assessing the protein expression of IFNAR1, IFNGR1, pROR1 (Tyr786), and ROR1 in vector-transduced and SLC22A10- and SLC22A15-OE clones treated with IFN-α-IFNα-R-I (10 μM) for 24 h β-Actin was used a loading control. Western blots shown represent three independent experiments.

Data in (J) were analyzed by one-way ANOVA with Dunnett's multiple comparisons test. $^{**}p < 0.01$; $^{***}p < 0.001$; ns, not significant. Results represent three independent experiments.

LV-SLC22A10, and LV-SLC22A15 to study changes in the gene expression. Principal component analysis separated DEGs identified by comparison of vector-transduced versus SLC22A10-OE clones and vector-transduced versus SLC22A15-OE clones. While evaluating the top DEGs, we identified Receptor Tyrosine Kinase-like Orphan Receptor 1 (*ROR1*), which has been established as a key contributor to EMT, metastasis, and stemness-associated drug resistance in various cancers, including breast, and ovarian, emerged as one of the top candidates. Moreover, an increased expression of EHF, UBE2U, HDAC9, ABCA1, NT5E, SLC20A1, and SCNN1A was observed. Notably, ROR1 transcripts were elevated in both SLC22A10- (9.16-fold) and SLC22A15-OE clones (10.22-fold) compared with the vector-transduced clones (Figures 4A–4C and Table S3). We also observed substantial increases in total and phosphorylated (at Tyr786) ROR1 proteins in both SLC22A10 and SLC22A15 clones compared with the vector-transduced clone (Figure 4D), which migrated between 100 and 130 kDa (Daneshmanesh et al., 2012). Furthermore, an ROR1 target, ALDH1A1, and ROR1-AS1 lncRNA were simultaneously increased in expression in both SLC22A10 and SLC22A15 clones (Zhang et al., 2014). Increased ROR1 expression and phosphorylation were also observed in HPAF-II stably overexpressing SLC22A10 and SLC22A15 (Figure 4D).

Although the role of ROR1 in promoting EMT has been studied in breast and ovarian cancers (Cui et al., 2013; Zhang et al., 2014), how ROR-1 maintains the malignant phenotypes leading to aggressiveness in pancreatic cancer is unknown. To investigate, we transduced PANC-1 cells with the lentiviruses harboring full-length ROR1 (pHAGE-ROR1) and evaluated the effect on EMT on these cells. Interestingly, pHAGE-ROR1-transduced PANC-1 cells showed increased mesenchymal characteristics with augmented cell scattering compared with the control cells (Figure 4E). The expression of the epithelial markers EpCAM, Keratin 8/18 and E-cadherin was decreased, and expression of the mesenchymal markers Twist-1, SLUG, Vimentin, and N-cadherin was concurrently increased (Figure 4F). To investigate whether ROR1 is required for the SLC22A-induced EMT in pancreatic cancer, we silenced ROR1 in SLC22A10- and SLC22A15-OE clones. The depletion of ROR1 levels substantially attenuated ROR1 phosphorylation (Tyr786) and the expression of key EMT transcription factors/mesenchymal markers Twist-1 and SLUG in both

SLC22A10- and SLC22A15-OE clones (Figure 4G). Collectively, these findings indicate that ROR1 is a putative mediator of SLC22A10- and SLC22A15-induced EMT and aggressiveness of pancreatic cancer cells.

To recognize the molecular signaling pathways accompanying SLC22A10- and SLC22A15-dependent ROR1 gene activation, we carried out gene set enrichment analysis (GSEA) using a hallmark gene set (Subramanian et al., 2007) and visualized the results with clusterProfiler (Yu et al., 2012). GSEA identified the IFN-α and IFN-γ signaling pathways as the top two pathways enriched by the overexpression of both SLC22A10 and SLC22A15 (Figures 4H and S3A). Indeed, several IFN-associated genes, such as *IFI44, OASL, and BST2*, were found to be common among the most upregulated genes by SLC22A10 and SLC22A15 (Figure S3B). The protein expression levels of interferon alpha/beta receptor 1 (IFNAR1), interferon gamma receptor 1 (IFNGR1), interferon regulatory factor 1 (IRF-1), and interferon regulatory factor 9 (IRF-9), which are key regulators of the IFN-α and IFN-γ signaling pathways, were increased in both SLC22-OE clones (Figure 4I). To investigate whether SLC22-OE cells also secrete IFNs into the extracellular media, we measured the level of both IFN-α and IFN-γ in the conditioned cell supernatants harvested from vector control, SLC22A10-OE and SLC22A15-OE clones, through ELISA. The levels of IFN-α and IFN-γ showed a non-significant increase in the secretome of SLC22A10-OE clones, whereas significantly higher levels of these cytokines (8.7-fold of IFN-α and 17.3-fold of IFN-γ) were detected in the supernatants of SLC22A15-OE clones compared with the vector-control clones, which suggests that these SLCs are capable of triggering IFN signaling pathway in a cell autocrine manner (Figure 4J).

Engagement of IFN ligands to the IFN receptors leads to the activation of the signal transducer and activator of transcription (STAT), which is considered as a master regulator of the EMT program. Inflammatory cytokines, particularly IFNs, are known to stimulate STAT3 signaling that supports pancreatic and other cancers (Corcoran et al., 2011; Edsbäcker et al., 2019). We found remarkable activation of pSTAT3 (phosphorylation at Tyr705) in SLC22A10- and SLC22A15-OE clones compared with the vector-transduced clone, but the total STAT3 expression level remained largely unchanged (Figure 4I). Notably, STAT3 has been demonstrated to bind the promoter of ROR1 and induce its transcriptional activation in two hematological malignancies (Hojjat-Farsangi et al., 2014; Li et al., 2010). Knockdown of both SLC22A10 and SLC22A15 in Mes PANC1 clones and Slc22a15 (Slc22a10 ortholog is absent in mice) in highly aggressive mouse *PDX-1-CRE, LSL-KRas*^{G12D}, LSL-Trp53$^{-/-}$ (mKPC) cells demonstrated a diminished ROR1 expression and phosphorylation with a reduced expression of IFN/STAT3 signaling members (Figure 4K).

Although IFNs were initially developed as therapeutics to activate immune cells against viral infection, the roles of IFN-α and IFN-γ in promoting metastasis have been implicated in many cancers (Lollini et al., 1993; Provance and Lewis-Wambi, 2019; Taniguchi et al., 1987; Zhu et al., 2014). We found that treatment with either IFN-α or IFN-γ amplified the IFN signaling-mediated STAT3 signaling pathway, leading to the activation of ROR1, in PANC-1 cells (Figure 4L). To determine whether the blockade of the STAT3 signaling pathway could suppress IFN signaling-mediated ROR1 activation, we treated the SLC22A10- and SLC22A15-OE clones with WP1066, a potent small-molecule inhibitor of the STAT3 signaling pathway (Ferrajoli et al., 2007). WP1066 treatment effectively inhibited ROR1 activation in SLC22A10-OE and SLC22A15-OE clones (Figure 4M). Furthermore, uncoupling IFN ligands to their receptors by treatment with IFN-α-IFNα-R interaction inhibitor (IFN-α-IFNα-R-I) effectively suppressed ROR1 activation in both SLC22-OE clones (Figure 4N). Taken together, these findings support that SLC22A10 and SLC22A15 activate IFN signaling in an STAT3-dependent manner to increase the ROR1 expression and promote PDAC EMT.

SLC22A10 and SLC22A15 support GSH accumulation to facilitate ROR1 activation

Because SLC22A10 and SLC22A15 are membrane-bound transporters that can aid in the biomolecule supply and/or metabolic rewiring seen in EMT, we next attempted to explore the metabolic alterations associated with the EMT and aggressiveness of the SLC22A10- and SLC22A15-OE clones. To this end, we performed untargeted metabolomics utilizing time-of-flight liquid chromatography-tandem mass spectrometry (Q-TOF LC-MS/MS) analyses (Liu et al., 2014). The samples prepared from vector, SLC22A10-, and SLC22A15-OE cell pellets were separated based on principal component analyses (Figure S3C). The pools of most differentially altered metabolites in the SLC22 clones compared with the vector were analyzed, followed by hierarchical clustering. Subsequent analyses revealed metabolites that were significantly increased in both SLC22A10- and SLC22A15-OE clones compared with the vector-transduced clone, particularly glutathione (GSH), oxiglutatione (GSSG), cysteinyl glycine, glutamyl cysteine glycine, cysteinyl glutamyl glycine and fructose 1,6-bisphosphate, among others. Glutaric acid, taurine, vitamin

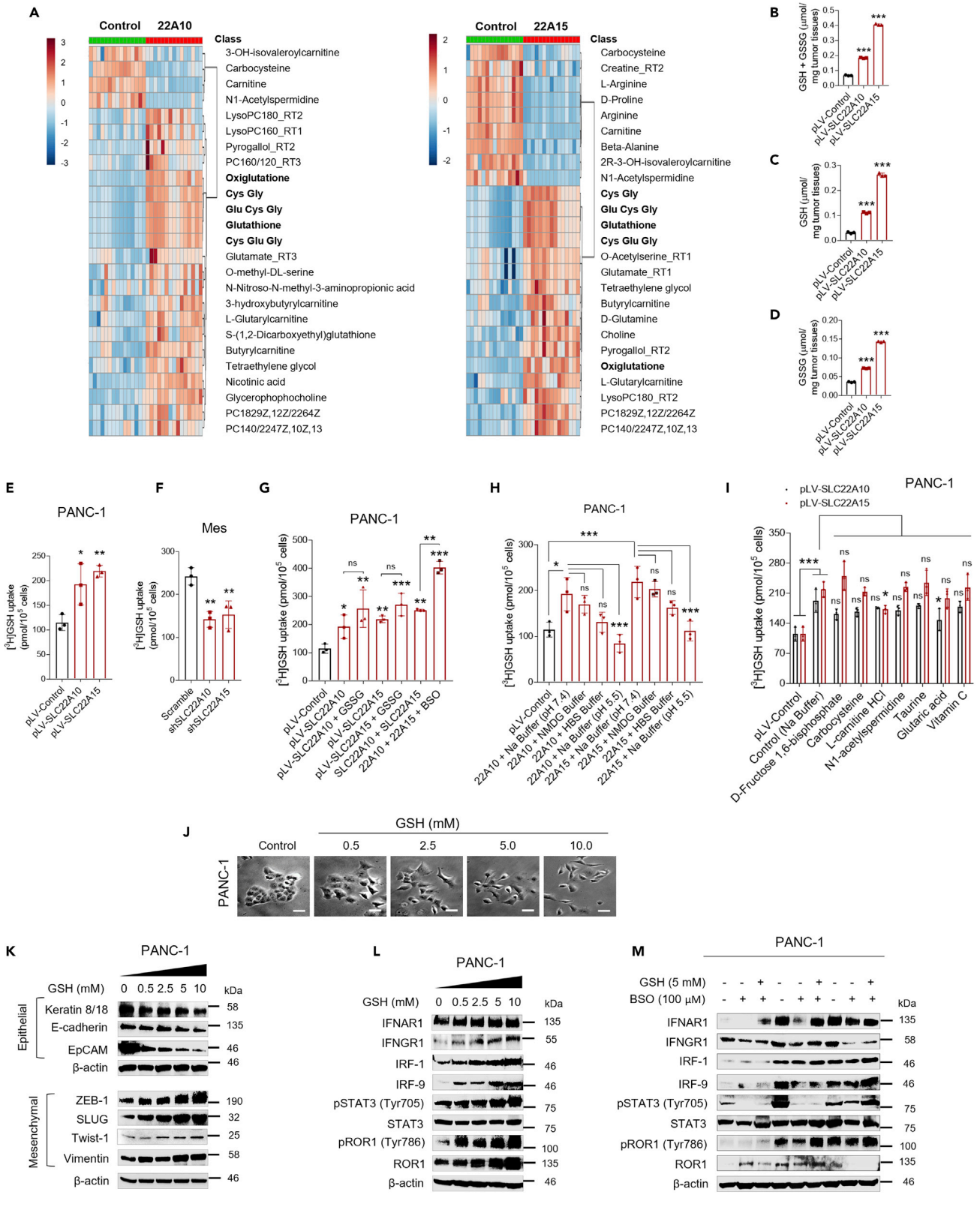
A
Control 22A10
Class
3-OH-isovaleroylcarnitine
Carbocysteine
Carnitine
N1-Acetylspermidine
LysoPC180_RT2
LysoPC160_RT1
Pyrogallol_RT2
PC160/120_RT3
Oxiglutatione
Cys Gly
Glu Cys Gly
Glutathione
Cys Glu Gly
Glutamate_RT3
O-methyl-DL-serine
N-Nitroso-N-methyl-3-aminopropionic acid
3-hydroxybutyrylcarnitine
L-Glutarylcarnitine
S-(1,2-Dicarboxyethyl)glutathione
Butyrylcarnitine
Tetraethylene glycol
Nicotinic acid
Glycerophophocholine
PC1829Z,12Z/2264Z
PC140/2247Z,10Z,13
Control 22A15
Class
Carbocysteine
Creatine_RT2
L-Arginine
D-Proline
Arginine
Carnitine
Beta-Alanine
2R-3-OH-isovaleroylcarnitine
N1-Acetylspermidine
Cys Gly
Glu Cys Gly
Glutathione
Cys Glu Gly
O-Acetylserine_RT1
Glutamate_RT1
Tetraethylene glycol
Butyrylcarnitine
D-Glutamine
Choline
Pyrogallol_RT2
Oxiglutatione
L-Glutarylcarnitine
LysoPC180_RT2
PC1829Z,12Z/2264Z
PC140/2247Z,10Z,13
B
GSH + GSSG (μmol/ mg tumor tissues)
pLV-Control
pLV-SLC22A10
pLV-SLC22A15
C
GSH (μmol/ mg tumor tissues)
D
GSSG (μmol/ mg tumor tissues)
E
PANC-1
[3H]GSH uptake (pmol/10^5 cells)
F
Mes
Scramble
shSLC22A10
shSLC22A15
G
PANC-1
[3H]GSH uptake (pmol/10^5 cells)
pLV-Control
pLV-SLC22A10
pLV-SLC22A10 + GSSG
pLV-SLC22A15
pLV-SLC22A15 + GSSG
SLC22A10 + SLC22A15
22A10 + 22A15 + BSO
H
PANC-1
[3H]GSH uptake (pmol/10^5 cells)
pLV-Control
22A10 + Na Buffer (pH 7.4)
22A10 + NMDG Buffer
22A10 + Na Buffer (pH 5.5)
22A10 + HBS Buffer
22A15 + Na Buffer (pH 7.4)
22A15 + NMDG Buffer
22A15 + HBS Buffer
22A15 + Na Buffer (pH 5.5)
I
PANC-1
pLV-SLC22A10
pLV-SLC22A15
[3H]GSH uptake (pmol/10^5 cells)
pLV-Control
Control (Na Buffer)
D-Fructose 1,6-bisphosphate
Carbocysteine
L-carnitine HCl
N1-acetylspermidine
Taurine
Glutaric acid
Vitamin C
J
GSH (mM)
Control
0.5
2.5
5.0
10.0
PANC-1
K
PANC-1
GSH (mM) 0 0.5 2.5 5 10
kDa
Epithelial
Keratin 8/18
E-cadherin
EpCAM
β-actin
Mesenchymal
ZEB-1
SLUG
Twist-1
Vimentin
β-actin
L
PANC-1
GSH (mM) 0 0.5 2.5 5 10
kDa
IFNAR1
IFNGR1
IRF-1
IRF-9
pSTAT3 (Tyr705)
STAT3
pROR1 (Tyr786)
ROR1
β-actin
M
PANC-1
GSH (5 mM)
BSO (100 μM)
kDa
IFNAR1
IFNGR1
IRF-1
IRF-9
pSTAT3 (Tyr705)
STAT3
pROR1 (Tyr786)
ROR1
β-actin

Figure 5. SLC22A10 and SLC22A15 transport glutathione that stimulates IFN-STAT3-ROR1 signaling and EMT

(A) Heat maps depicting metabolites that are significantly altered in SLC22A10-OE (left panel) and SLC22A15-OE (right panel) clones compared with the vector-transduced clone, as determined by untargeted metabolomics utilizing LC-MS/MS in ESI + mode. Metabolites in bold are related and significantly increased in both SLC22A10- and SLC22A15-OE clones compared with the vector-transduced clone. $n = 5$ biological replicates and $n = 3$ technical replicates of each sample (pLV-Control, pLV-SLC22A10, and pLV-SLC22A15) were analyzed.

(B–D) Levels of total cellular glutathione (GSH + GSSG), reduced glutathione (GSH), and oxidized glutathione (GSSG) in primary tumor tissues dissected from mice described in Figure 2 G. Error bars, mean ± SD. Tissues from $n = 3$ tumors for each condition was processed and assayed.

(E) Transport of radiolabeled [glycine-2-^{3}H]-glutathione was determined in PANC-1 cells transduced with control, SLC22A10, and SLC22A15 lentiviruses. Error bars, mean ± SD.

(F) Transport of [glycine-2-^{3}H]-glutathione in Mes cells transduced with scramble, shSLC22A10, and shSLC22A15 lentiviruses. Error bars, mean ± SD.

(G) Transport of [glycine-2-^{3}H]-glutathione in PANC-1 cells transduced with control, SLC22A10, and SLC22A15 lentiviruses or co-transduced with SLC22A10 and SLC22A15 lentiviruses. Cells were pretreated with BSO (100 μM) for 24 h before the transport study. GSSG (20 mM) was added to the transport buffer for the duration of transport period. Error bars, mean ± SD.

(H) Transport of [glycine-2-^{3}H]-glutathione in the presence of Na^+-containing buffer at pH 7.4 or N-methyl-D-glucamine chloride (NMDG) buffer or HEPES buffered saline (HBS) or Na^+-containing buffer at pH 5.5 in PANC-1 cells transduced with control, SLC22A10, and SLC22A15 lentiviruses. Error bars, mean ± SD.

(I) Transport of [glycine-2-^{3}H]-glutathione in PANC-1 cells transduced with control, SLC22A10, and SLC22A15 lentiviruses in the presence of 100 μM each of top differentially altered metabolites (identified from the metabolomic analysis of pLV-Control, pLV-SLC22A10, and pLV-SLC22A15 clones). For the data presented in (E–I), three biological replicates for each condition were tested and $n = 3$ independent experiments were performed.

(J) Representative phase contrast images of PANC-1 cells treated with indicated concentrations of GSH for 48 h. Scale bar, 50 μm. Three random fields from each condition were photographed and analyzed. $n = 3$ independent experiments performed.

(K) Western blots depicting the protein expression of epithelial and mesenchymal markers in PANC-1 cells treated with indicated concentrations of GSH for 6 h β-Actin were used as a loading control. Western blots shown represent three independent experiments.

(L) Western blots illustrating the protein expression of the markers of IFN-STAT3-ROR1 signaling axis in PANC-1 cells treated with increasing concentrations of GSH for 6 h β-Actin were used as a loading control. Western blots shown represent three independent experiments.

(M) Western blots assessing the protein expression of markers of the IFN-STAT3-ROR1 signaling axis in vector-transduced and SLC22A10- and SLC22A15-OE clones treated with the indicated concentrations of BSO and GSH. Cells were treated with BSO or vehicle for 24 h and followed by GSH or vehicle for 6 h β-Actin was used as a loading control. Western blots represent at least three independent experiments.

Data presented in (B–G) were analyzed by one-way ANOVA with Dunnett's multiple comparisons test and data presented in (H and I) were analyzed by two-way ANOVA with Dunnett's multiple comparisons test. *$p < 0.05$; **$p < 0.01$; ***$p < 0.001$; ns, not significant.

C, carnitine, carbocysteine, and N1-acetylspermidine were among the most downregulated metabolites in both SLC22A clones (Figures 5A and S3D; Table S4). There were also other metabolites that did not overlap in SLC22A10- and SLC22A15-OE cells. The enrichment of glutathione and its oxidative disulfide derivative (GSSG) with di- and tripeptides of amino acids present in GSH in both the SLC22A10- and SLC22A15-OE clones was compelling; therefore, to validate the results of untargeted metabolomics analysis, we directly measured changes in the levels of GSH and GSSG in tumor tissues derived from these clones (Figure 2G) via a quantitative colorimetry-based glutathione assay. Interestingly, as shown in Figures 5B–5D, the levels of the total intracellular glutathione (GSH + GSSG), GSH and GSSG, were higher by ≥ 2-fold in mouse pancreatic tumors derived from both SLC22A10- and SLC22A15-OE clones compared with the vector-transduced clone.

As excess GSH accumulated in SLC22A10- and SLC22A15- cells and SLC22-OE-derived mouse pancreatic tumors and GSH can exist in different species (neutral, anionic, zwitterionic), we examined whether GSH is a cargo of SLC22A10 (an organic anion transporter) or SLC22A15 (an organic cation transporter). We treated vector-transduced and SLC22A-OE cells with radiolabeled [glycine-2-^{3}H]-GSH and determined differences in the cellular accumulation of the labeled GSH over time. The transport of [glycine-2-^{3}H]-GSH was augmented (1.67- to 1.9-fold) in both the SLC22A10- and SLC22A15-OE cells compared with the vector-transduced cells (Figure 5E) without changes in transport of L-glutamic acid, a constituent amino acid of GSH (Figure S3E). Lentiviral transduction of shRNAs against SLC22A10 and SLC22A15 reduced the uptake of ^{3}H-labeled GSH in aggressive Mes cells (Figure 5F). Although the observed fold increases in GSH transports in SLC22A-OE cells were modest, the simultaneous overexpression of SLC22A10 and SLC22A15 further increased on ^{3}H-GSH transport (increased to 2.23- to 2.35-fold) when compared with that seen with OE of the individual SLCs. Moreover, the magnitude of GSH transport was further stimulated when endogenous GSH levels in these cells were depleted by pretreatment with buthionine-[S, R]-sulfoximine (BSO) (increased to 3.5-fold), a potent inhibitor of cellular GSH biosynthesis (Harris et al., 2015), in cells OE both SLC22A10 and SLC22A15 compared with the vector-transduced cells (Figure 5G). The maximal uptake of GSH was observed in Na^+-containing buffer at pH 7.4, not Na^+-free buffer (contains N-methyl-D-glucamine chloride instead of NaCl) or HEPES buffered saline (HBS) or Na^+-containing buffer at pH 5.5, suggesting SLC22A10 and SLC22A15 can accumulate GSH inside pancreatic cancer cells at blood

pH and salinity (Figure 5H). Furthermore, none of the other top differentially altered metabolites competitively inhibited SLC22A10/15-mediated GSH uptake into pancreatic cancer cells (except for a minor inhibition by carnitine) (Figure 5I). Together, these findings suggest that GSH is a cargo of SLC22A10 and SLC22A15 and that cooperativity between SLC22A10 and SLC22A15 increases intracellular GSH levels in pancreatic cancer cells. Moreover, the results show that the re-establishment of GSH levels in PANC-1 cells OE SLC22A10 and SLC22A15 was achievable after the loss of endogenous synthesis of GSH.

High intracellular GSH levels have been implicated in cancer cell survival and therapeutic resistance in recent years (Bansal and Simon, 2018); however, whether GSH plays a direct role in EMT and pancreatic cancer metastasis is unclear. To address this, we treated PANC-1 cells with intratumoral concentrations of GSH (~5–10 mM) (Xiong et al., 2021) and examined its effect on EMT. Intriguingly, EMT-associated morphometric changes, including an increase in cell scattering and more elongated cellular morphology, were evident in these cells at that concentration (Figure 5J). Furthermore, the expression of several epithelial markers was downregulated with the concomitant upregulation of mesenchymal markers in PANC-1 cells when these cells were treated with GSH in a dose-dependent manner (Figure 5K). Notably, we observed the substantial activation of pROR1 (Tyr786) with the elevated expression of IFN signaling molecules in PANC-1 cells exposed to increasing concentrations of GSH (Figure 5L). To investigate whether the endogenous synthesis of GSH also promotes the IFN signaling pathway in SLC22-OE clones, we depleted endogenous GSH in these clones by pretreatment with BSO for 24 h, followed by their exposure to GSH treatment for 6 h. Immunoblot analysis of whole-cell lysates revealed that BSO treatment distinctly inhibited several players of IFN signaling and ROR1 activation in the SLC22A10- and SLC22A15-OE clones and exogenously supplemented GSH reversed the inhibitory effects of BSO by partially or fully restoring their expression and reestablishing ROR1 phosphorylation levels in SLC22-OE clones (Figure 5M). Taken together, these findings further support the transport and accumulation of extraneous GSH augments IFN-STAT3-ROR1 signaling in SLC22A10- and SLC22A15-OE pancreatic cancer cells.

The increased expression of SLC22A15 in pancreatic stromal tissues compared with the normal pancreatic tissues suggested a possible stromal augmentation of pro-EMT characteristics of SLC22A15 in human pancreatic cancers as well. Indeed, PDACs are characterized by intense desmoplastic stroma comprised of activated fibroblasts, endothelial cells, immune cells, and the extracellular matrix. Pancreatic cancer-associated fibroblasts (PCAFs) are the critical stromal components as they secrete soluble factors involved in PDAC progression and chemoresistance (Pereira et al., 2019; Provenzano et al., 2012). Interestingly, the SLC22A15 expression was observed in normal pancreatic stellate cells (PSCs) consistent with the expression noted in stellate cells surrounding normal pancreatic acinar tissue (Figure 3B). No expression of SLC22A10 was detected in either PCAFs or PSCs. The SLC22A15 expression was significantly higher in PCAFs than observed in PSCs as observed by Western blotting analysis of total cell lysates and was predominantly localized at the cell surface as observed by immunocytochemical analysis (Figures S4A–S4C). When the intracellular GSH levels in normal PSCs and PCAFs were measured, we noted considerably higher levels of total GSH (GSH + GSSG) and oxidized glutathione (GSSG) in PCAFs compared with that in PSCs (Figure S4D). Similarly, we found elevated concentrations of GSH + GSSG, GSSG, and GSH in the conditioned medium (CM) from PCAFs (PCAFs-CM) compared with the CM from PSCs (Figure S4E). Remarkably, an increase in GSH levels in PCAFs correlated with augmented IFN-signaling via the STAT3/ROR1 signaling axis (Figure S4F). Intriguingly, amplification of IFN signaling in PANC-1 cells was observed within 4 h of exposure to PCAFs-CM, suggesting GSH-stimulated, stromal cell augmentation of IFN signaling in pancreatic cancer cells occurs in a paracrine manner (Figures S4G and S4H).

Lesinurad reduces metastasis and chemoresistance in mouse models of PDAC

The increased accumulation of GSH in SLC22A10/15-OE clones (and tumors derived from those clones) and the higher transport of [glycine-2-^{3}H]-GSH in Mes clones: 2.7-fold compared with Epi clones (Figure S5A) supporting IFN/STAT3/ROR1 signaling axis suggest that the aggressiveness of Mes clones is followed by increased GSH transport. To discover potential inhibitor(s) of the GSH transport that could curtail the IFN/STAT3/ROR1 signaling and EMT in PDAC, we screened known pharmacological inhibitors of the SLC22 family of transporters, including semisynthetic and naturally occurring inhibitors of OAT-1, OAT-3, and URAT-1 transporters (probenecid, verinurad, benzbromarone, sulfinpyrazone, lesinurad, novobiocin, morin, luteolin, and steviol) (An et al., 2014; Duan and You, 2009; Koepsell, 2013; Sanchez-Niño et al., 2017; Tan et al., 2016, 2017). Interestingly, lesinurad and novobiocin showed competency in inhibiting

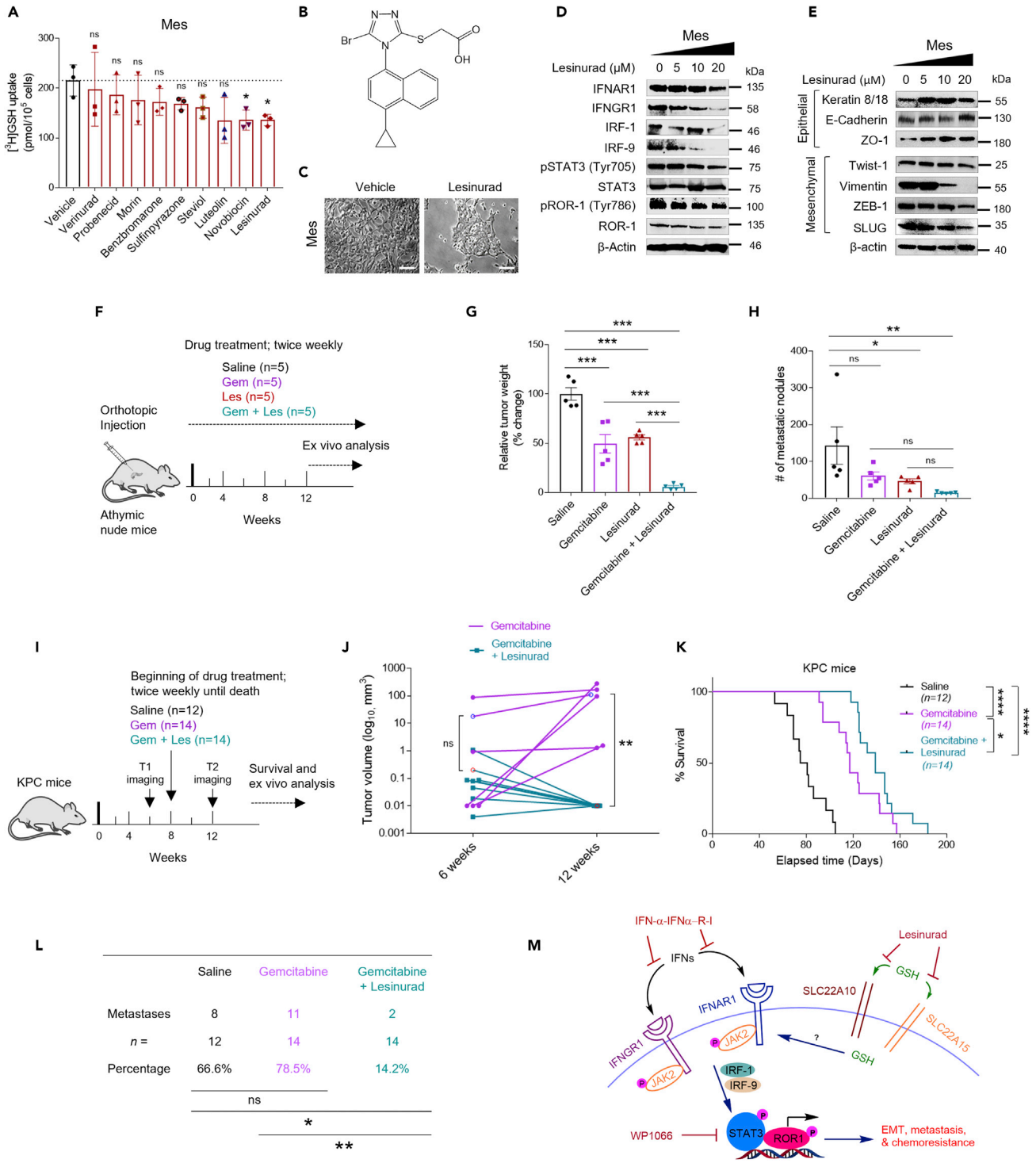

Figure 6. Lesinurad, an SLC22 inhibitor suppressed IFN signaling and EMT in Mes cells and in combination with gemcitabine restrained tumor growth, and metastasis in mouse models of PDAC

(A) Transport of [glycine-2-^{3}H]-glutathione measured in the presence of SLC22 inhibitors (20 μM each) in Mes cells. Error bars, mean ± SD. *n* = 3 biological replicates for each condition was examined and three independent experiments were performed.

(B) Structure of lesinurad.

(C) Representative phase contrast images of the Mes cells treated with vehicle or lesinurad (20 μM) for 48 h. Scale bar, 50 μm *n* = 5 random fields from each condition was photographed and analyzed and data represent three independent experiments.

Figure 6. *Continued*

(D) Western blots showing the protein expression of players in the IFN-STAT3-ROR1 signaling axis in Mes clones treated with indicated concentrations of lesinurad for 48 h β-Actin was used as a loading control.

(E) Western blots illustrating the protein expression of epithelial and mesenchymal markers in Mes clones treated with indicated concentrations of lesinurad for 48 h β-Actin was used as a loading control. Data presented in (D and E) represent three independent experiments.

(F) Design of an orthotopic mouse pancreatic tumor xenograft study conducted to evaluate the anti-tumor and antimetastatic abilities of gemcitabine and lesinurad alone and the combination of both drugs at the indicated doses detailed in the STAR Method section.

(G) Quantification of weights of the primary tumors dissected from above groups of animals. Error bars, mean ± SEM. $n = 5$ mice per group; each point represents one animal.

(H) Quantification of metastatic foci in the viscera and cavities from the above groups of animals. Tumor associated metastatic foci and lesions >1 mm^3 were scored and included in the analysis. Error bars, mean ± SEM. $n = 5$ mice per group; each point represents total number of metastatic nodules quantified from one animal.

(I) Design showing KPC mice study conducted to assess the efficacy of gemcitabine alone and in combination with lesinurad on survival, tumor growth, and metastasis.

(J) Changes in individual tumor volumes at 6 (T1) and 12 weeks of age (T2) as determined by micro-CT imaging analyses. Animals that received gemcitabine alone ($n = 5$ tumors) versus the combination of gemcitabine + lesinurad ($n = 7$ tumors) are compared. Each line represents one tumor and the average change in the collective tumor volume is presented in lines with open circles. $n = 3$ KPC mice per group were monitored by micro-CT imaging for tumor burden.

(K) Kaplan–Meier survival analysis showing the elapsed survival time of groups of KPC mice treated with saline ($n = 12$ mice), gemcitabine ($n = 14$ mice), or gemcitabine + lesinurad ($n = 14$ mice) at the indicated doses (detailed in STAR Method section) twice a week.

(L) The incidence of metastasis in KPC mice enrolled in the saline ($n = 12$ mice), gemcitabine monotherapy ($n = 14$ mice), and gemcitabine + lesinurad groups ($n = 14$ mice), as determined by post-survival necropsy examination.

(M) Model of the proposed mechanism of action of SLC22A10 and SLC22A15 in promoting EMT and pancreatic cancer progression.

Data in (A) were analyzed by one-way ANOVA with Dunnett's multiple comparisons test. Data in (G and H) were analyzed by one-way ANOVA with Tukey's multiple comparisons test. Data in (J) were analyzed by two-way ANOVA with Sidak's multiple comparisons test. For the data presented in (K), the differences in median overall survival times of KPC mice in different groups were analyzed using log rank (Mantel–Cox) test. Data presented in (L) were analyzed by Fisher's exact test. *$p < 0.05$; **$p < 0.01$; ***$p < 0.001$; ****$p < 0.0001$; ns, not significant.

the transport of [glycine-2-^{3}H]-GSH in Mes clones (Figure 6A). Moreover, lesinurad and steviol blocked the transport of *p*-aminohippuric acid (^{3}H-PAH), a prototypic substrate of SLC22 transporters, in Mes clones (Figure S5B). Treatment of Mes clones with lesinurad inhibited cell scattering while increasing cell-cell adhesion and epithelial morphology (Figures 6B and 6C). Intriguingly, the protein expression of several IFN signaling molecules (IFNAR1, IFNGR1, IRF-1, IRF-9), pSTAT3, and pROR1 was suppressed with increasing doses of lesinurad in Mes clones (Figure 6D). In addition, lesinurad inhibited EMT characteristics with the induction of epithelial markers and downmodulation of mesenchymal markers (Figure 6E). Lesinurad also potently impeded the migratory and invasive abilities of Mes clones (Figures S5C and S5D). Furthermore, lesinurad attenuated the paracrine signaling imparted by PCAFs on PANC-1 cells; we observed downmodulation of IFN signaling pathway players in PANC-1 cells cultured in presence of the CM collected from PCAFs treated with lesinurad (Figure S5E). These results suggest that a pan-SLC22A inhibitor lesinurad blocks GSH transport and accumulation in the tumor cells to inhibit the oncogenic IFN/ROR1 signaling in PDAC.

The drug gemcitabine currently used in the treatment of pancreatic cancer is shown to have limitations in that most pancreatic cancers exhibit refractoriness to gemcitabine and gemcitabine itself increases the EMT characteristics and metastatic incidences of PDAC. Furthermore, recent studies show the inhibition of EMT *in vivo* can increase the effectiveness of nucleoside analogs such as gemcitabine (Zheng et al., 2015). To assess the chemotherapeutic effects of SLC22A10 and SLC22A15 inhibition on EMT-associated metastasis and gemcitabine chemoresistance, we tested the *in vivo* efficacy of lesinurad in combination with gemcitabine, in Foxn1"nu" mice orthotopically implanted with Mes clones in the pancreas. Two weeks after tumor cell implantation, gemcitabine or lesinurad, or both, were administered (25 mg each/kg IP), which continued twice weekly for the duration of the experiment (Figure 6F). As single agents, both gemcitabine and lesinurad restricted tumor growth in the highly aggressive Mes clones implanted into athymic nude mice, whereas additive regression of tumor growth was achieved in the group of animals treated with both these drugs in combination (Figures 6G and S5F). Furthermore, the combination of gemcitabine and lesinurad decreased the formation of gross and microscopic metastatic foci in the liver, spleen, peritoneum, kidney, and intestines compared with those in mice treated with saline or gemcitabine alone (Figure 6H). Mice treated with lesinurad and gemcitabine in combination did not exacerbate toxicity or exhibit any noticeable adverse effects such as loss of muscle mass, whereas saline-treated animals became cachectic with significantly lower tumor-corrected body weight at 12 weeks (Figure S5G).

As LSL-KrasG12D/+; LSL-Trp53R172H/+; Pdx-1-Cre mice dynamically recapitulate the tumor microenvironment (TME) in human PDAC with respect to tumor-stromal organization and anti-tumor immune response not achievable in orthotopic models (Provenzano et al., 2012; Steele et al., 2016), we further tested the efficacy of the combination of gemcitabine + lesinurad in comparison with that of gemcitabine as a single agent in a similar strain of mice, LSL-KrasG12D/+; LSL-Trp53R270H/+; Pdx-1-Cre (KPC) mice (Shakya et al., 2013). Gemcitabine, alone and in combination with lesinurad, was administered (25 mg each/kg IP) twice weekly to age-matched and randomly segregated KPC mice starting at eight weeks of age for until the early removal criteria was met (Figure 6I). After 6 (T1) and 12 (T2) weeks, when several individual tumors in the two treatment groups were tracked and quantified by high-resolution micro computed tomography (micro-CT) imaging and analyses, tumor growth was significantly reduced in animals in the gemcitabine + lesinurad group compared with those in the gemcitabine group (Figures 6J and S5H). Interestingly, the median overall survival increased from 78 days in the control (saline) group to 117 days in the gemcitabine monotherapy group to 139 days in the gemcitabine + lesinurad group (43.88% and 15.82% increase in survival in the combination group compared with the saline treated group and gemcitabine treated group, respectively) (Figure 6K). Further, necropsy examination of mice in the gemcitabine + lesinurad group displayed lower incidence of tumor burden and metastasis than animals in the gemcitabine or saline group (Figures 6L and S5I). Thus, the combination of lesinurad and gemcitabine enhanced gemcitabine chemosensitivity, reduced the tumor and metastatic burden, and increased the overall survival in a spontaneous mouse model of PDAC.

DISCUSSION

The study revealed two less characterized transporters from the organic anion/cation transporter family that contribute to EMT in pancreatic cancer, SLC22A10 and SLC22A15. These findings uncover the unexpected role of what are generally considered as renal and hepatic solute carrier transporters (SLC22A) in pancreatic tumorigenicity. The findings are however consistent with some other recent findings such as the glutamine deprivation-induced EMT in PDAC where both SLC22A10 and SLC22A15 are found increased in pancreatic cancer (Recouvreux et al., 2020) and SLC22A15 has been found to increase tumorigenicity in colon cancer (Zhu et al., 2019) and required for the invasion and migration of hepatocellular carcinoma cells (Fang et al., 2021). Together, these findings identify the emerging roles of distinct SLC22A transporters in tumor progression (Jung et al., 2015). Mechanistically, SLC22A10 and SLC22A15 were shown to augment the GSH-supported IFN/STAT3/ROR1 signaling and activate EMT, metastasis, and chemoresistance in pancreatic cancer cells. Genetic or pharmacological targeting of SLC22A10 and SLC22A15 partially interfered with EMT-driven metastasis and chemoresistance by potentially halting the SLC22A transport and their dependent oncogenic signaling in orthotopic and spontaneous mouse pancreatic cancer models. Collectively, our findings reveal a new association of SLC22A10 and SLC22A15 with EMT-associated metastasis and chemoresistance in pancreatic cancer and expose tumor cell vulnerabilities that could be targeted for therapeutic intervention in pancreatic cancer.

IFNs play a dual (with both immunostimulatory and immunosuppressive effects) role in cancer depending on the IFN-stimulatory genes transcribed, tumor type, and context (Minn, 2015). Type-I IFNs, particularly IFN-α, have been implicated in promoting migration and drug resistance in inflammatory breast cancer (Provance and Lewis-Wambi, 2019), whereas in PDAC, IFN-α inhibits tumor growth but augments metastasis and increases expression of the cancer stem cell markers CD24, CD44, and CD133 *in vitro* as well as *in vivo* (Zhu et al., 2014). Likewise, ample evidence has revealed the positive role of IFN-γ in immune evasion and metastasis in multiple cancers (Mojic et al., 2018; Zaidi, 2019). For example, IFN-γ activates EMT in pancreatic cancer by augmenting the expression of vimentin and IRF-1 and STAT-1 phosphorylation, which correlate with poor patient prognosis (Imai et al., 2019). Treatment of mice with IFN-γ induced the lung colonization of B16 melanoma cells, and transfection of the IFN-γ gene into TS/A mammary adenocarcinoma cells spontaneously increased metastases in BALB/c mice (Lollini et al., 1993; Taniguchi et al., 1987). Other studies have documented the roles of IFN-γ in stimulating the development of papilloma and colorectal carcinomas (Hanada et al., 2006; Xiao et al., 2009). Our findings support IFN signaling are indeed important for the transformation of cancer cells, and demonstrate that SLC22A10- and SLC22A15-OE clones are enriched in both the IFN-α and IFN-γ signaling pathways, supporting the EMT phenotypes of pancreatic cancer.

ROR1, an embryonic protein, is frequently overexpressed and promotes EMT, invasion, and migration in multiple cancers, including triple-negative breast cancer, ovarian cancer, and chronic lymphocytic

leukemia (Cui et al., 2013, 2016; Zhang et al., 2014). Although the ROR1 expression has been documented in pancreatic islets, circulating tumor cells, and pancreatic tumor tissues (Balakrishnan et al., 2017), the mechanism of ROR1 activation and its implications for EMT in pancreatic cancer remained unclear. Our findings suggest ROR1 is a target of SLC22A10- and SLC22A15-induced IFN signaling in mesenchymal pancreatic cancer cells, which contribute to their EMT effects. The binding of IFN-α and IFN-γ to the corresponding receptors (IFNAR1 and IGNGR1, respectively) triggers the activation of both STAT1 and STAT3 (Qing and Stark, 2004; Velichko et al., 2002). In pancreatic cancer, STAT3 is necessary for modification of the tumor stroma to facilitate tumor growth and gemcitabine resistance (Wörmann et al., 2016). Our results revealed the elevated expression of key molecules of the type-I and type-II IFN signaling pathways, IFNAR1, IFNGR1, IRF-1, and IRF-9, with the activation of STAT3 in the SLC22A10- and SLC22A15-OE clones, whereas treatment with inhibitors of STAT3 or IFN/IFN receptor interaction reduced this activity. The activation of STAT3 stimulates a number of downstream oncogenic molecules and transcription factors, directing tumor cell proliferation, and EMT, supporting the malignant phenotypes of pancreatic cancer (D'Amico et al., 2018). ROR1 is crucial among STAT3 target genes (Tseng et al., 2010) and the ROR1 promoter harbors IFN-γ activation sequence-like elements, which are predominantly activated by STAT3 (Hojjat-Farsangi et al., 2014; Li et al., 2010; Rozovski et al., 2019). Together, our findings provide support for SLC22A10 and SLC22A15 activation of IFN/STAT3/ROR1 signaling to favor EMT in pancreatic cancer (Figure 6M).

GSH, the most abundant physiological antioxidant, has been implicated in tumor growth, metastasis, and therapeutic resistance (Bansal and Simon, 2018; Estrela et al., 2016). Conversely, the GSH synthesis inhibitor BSO has shown preclinical and clinical therapeutic effects to enhance the efficacy of chemotherapy and radiotherapy against diverse cancers (Harris et al., 2015; Tagde et al., 2014). Our data establish that SLC22A10- and SLC22A15-expressing pancreatic tumor cells are enriched in GSH that also correlates with the increased transport activities of SLC22A10 and SLC22A15 that can accumulate GSH inside pancreatic cancer cells (Figures 5A–5G and S3D). Furthermore, GSH itself promotes IFN signaling and ROR1 activation when pancreatic cancer cells are treated with extraneous GSH concentrations relevant to pancreatic TME. Moreover, SLC22A10 and SLC22A15 compensate for any loss of intracellular biosynthesis of GSH, thereby identifying a crosstalk between the GSH synthetic and transport activities in promoting EMT of PDAC. Whether GSH directly activates IFN signaling in PDAC is unclear, however, earlier studies have shown that glutathione peroxidase 4 maintains redox homeostasis that can activate stimulator of interferon gene (STING) and interferon pathway-associated genes (Jia et al., 2020; Tao et al., 2020). We found significant upregulation of STING1 and interferon stimulatory genes (ISGs) including ISG15, OASL, and IFI44 in the RNA sequencing analysis of SLC22A10- and SLC22A15-OE clones (Figure S3F). Beyond the tumor cell intrinsic contributions of SLC22A10 and SLC22A15, our findings also suggest the presence of tumor cell extrinsic activity of SLC22A15 in regulating EMT and pancreatic tumor progression. For instance, a high expression of SLC22A15 was observed in the stromal compartments of human PDAC tissues and pancreatic cancer associated fibroblasts, which suggests SLC22A15 is particularly activated in the PDAC stroma to promote EMT. Priming of parenchymal tumor cells with media derived from pancreatic cancer stromal cell cultures induced GSH-activated IFN/STAT3/ROR1 signaling, which provided further evidence for the presence of SLC22A15-mediated paracrine signaling activating EMT. Rationally, we postulate that elevated GSH levels trigger IFN signaling in the SLC22A10- and SLC22A15-OE clones to support the EMT program in pancreatic cancer.

Through the combination of our rational screening of a panel of small-molecule inhibitors of the SLC22 family, our studies identified lesinurad as an inhibitor of SLC22A10 and SLC22A15 that abrogated EMT in Mes pancreatic clones. Although the Federal Drug Administration (FDA) has approved lesinurad in combination with allopurinol (a xanthine oxidase inhibitor) for the treatment of patients with gout-associated hyperuricemia (Abramowicz et al., 2018), there are no reports on its clinical utility for cancer therapy. The current study provides proof-of-principle evidence that pharmacological inhibition of SLC22A transporters by lesinurad reduces the transport of GSH and restrains the activation of the IFN/STAT3/ROR1 signaling-induced EMT pathway in aggressive pancreatic cancer cells. Moreover, in combination with the existing standard of care gemcitabine, lesinurad significantly suppressed tumor growth and metastatic burden in Mes clone-induced mouse orthotopic pancreatic tumor xenografts, reflecting its potential synergistic and chemosensitizing effects. Furthermore, the combination of gemcitabine and lesinurad reduced metastatic burden and prolonged survival in *Kras* and *Trp53* mutated mice with spontaneously developed tumors and metastatic disease, warranting lesinurad's repurposing and clinical testing in patients with advanced pancreatic cancer.

Limitations of the study

The study utilizes a cell line-based EMT model where cells exist in either epithelial state or mesenchymal state. Because EMT is a dynamic event, it would be worthwhile to confirm our findings in other EMT models that encompasses various epithelial-mesenchymal hybrid states. The study suggests that SLC22A10 and SLC22A15 exert their pro-EMT and tumorigenic effect through overlapping mechanisms involving GSH. However, our data also identify other metabolites that are either enriched or depleted in SLC22A10-OE and SLC22A15-OE cells that do not overlap. The observation that KD of SLC22A10 or SLC22A15 has a substantial effect on tumor growth and EMT markers is also compatible with the possibility that these carriers transport non-overlapping substrates that affect tumor progression via mechanisms further downstream. Furthermore, how GSH activates IFN and/or ROR1 signaling mechanistically is not fully known and needs to be explored in relevance to PDAC. Subsequent investigations using transporter-deficient PDAC models (e.g., Slc22a15 KO mice on a KPC background) are expected to clarify the role of SLC22A10 and SLC22A15 in pancreatic cancer progression and treatment resistance. Finally, owing to the lack of specific inhibitors for SLC22A10 or SLC22A15, the study utilized a pan-SLC22A inhibitor to test the effects on the KPC model. The identification of more potent and specific inhibitors of SLC22A10 and SLC22A15 in PDAC may also be of interest in the future.

STAR★METHODS

Detailed methods are provided in the online version of this paper and include the following:

- KEY RESOURCES TABLE
- RESOURCE AVAILABILITY
  - Lead contact
  - Material availability
  - Data and code availability
- EXPERIMENTAL MODEL AND SUBJECT DETAILS
  - Mouse models and ethics statement
  - Normal human tissue samples and human pancreatic tumor microarray
  - Cell lines and culture conditions
- METHOD DETAILS
  - Lentiviral transduction and generation of stable cell lines
  - RNA-seq, differential expression analysis and gene set enrichment analysis
  - Unbiased metabolomic profiling and analysis
  - [^{3}H] radionuclide transport assay
  - Glutathione measurements
  - Quantification of IFN-α and IFN-γ by ELISA
  - Real-time qPCR
  - Western blotting
  - Immunocytochemistry
  - Transwell cell migration and invasion assays
  - Pharmacological inhibitors and formulation preparation
  - Orthotopic pancreatic tumor xenograft model
  - KPC mice treatment regimens and survival analyses
  - μCT imaging of KPC animals
  - Multiplexed immunohistochemistry of TMA
  - IHC image quantification and analysis
- QUANTIFICATION AND STATISTICAL ANALYSIS

SUPPLEMENTAL INFORMATION

Supplemental information can be found online at https://doi.org/10.1016/j.isci.2022.104193.

ACKNOWLEDGMENTS

The research reported in this publication was funded by the National Institutes of Health (1RO1CA188464, R01GM143217) and a Research Scholars Grant (RSG-15-036-01-DDC) from the American Cancer Society awarded to R.G. Resources and analyses presented in this report were generated using the shared resource facilities at The Ohio State University and Ohio State University Comprehensive Cancer Center (OSUCCC).

These facilities are supported in part by grant P30CA016058 from the National Cancer Institute, Bethesda, MD. The content of this study is solely the responsibility of the authors and does not necessarily represent the official views of the National Institutes of Health. We thank Target Validation Shared Resource, OSUCCC, for the generation of KPC mice and Small Animal Imaging Core, OSUCCC for micro-CT and IVIS imaging of the experimental mice. We acknowledge Campus Chemical Instrument Center (CCIC) Mass Spectrometry and Proteomics (MS&P) Facility services and resources at The Ohio State University for their assistance in performing metabolomic analyses. We appreciate Genomics Services Core, The Research Institute at Nation-wide Children's Hospital, Columbus, Ohio, for conducting RNA sequencing. We thank Anusha Singh and Shreya Barde for their technical assistance. Finally, the authors express gratitude to the Pelotonia Fellowship Program, OSUCCC – James for predoctoral and post-doctoral fellowships to A.K.P. and D.N., respectively.

AUTHOR CONTRIBUTIONS

D.N., B.W., A.K.P., and R.R. performed the experiments. D.N., B.W., J.L., M.J.C., and R.G. analyzed the data. D.N., B.W., M.J.C., and R.G. investigated the study. R.G. and R.S. provided the resources. D.N. wrote the original draft of the manuscript. R.G. conceptualized the project, supervised the study, and edited the manuscript. All authors reviewed the final manuscript.

DECLARATION OF INTERESTS

The authors declare no potential conflicts of interests.

INCLUSION AND DIVERSITY

We worked to ensure sex balance in the selection of non-human subjects. We worked to ensure diversity in experimental samples through the selection of the cell lines. The author list of this paper includes contributors from the location where the research was conducted who participated in the data collection, design, analysis, and/or interpretation of the work.

Received: February 9, 2021
Revised: January 31, 2022
Accepted: March 30, 2022
Published: May 20, 2022

REFERENCES

Abramowicz, M., Zuccotti, G., and Pflomm, J.-M. (2018). Lesinurad/allopurinol (duzallo) for gout-associated hyperuricemia (reprinted from the medical letter on drugs and therapeutics vol 59, pg 182-183, 2017). JAMA *319*, 188–189.

Aiello, N.M., Brabletz, T., Kang, Y., Nieto, M.A., Weinberg, R.A., and Stanger, B.Z. (2017). Upholding a role for EMT in pancreatic cancer metastasis. Nature *547*, E7.

An, G., Wang, X., and Morris, M.E. (2014). Flavonoids are inhibitors of human organic anion transporter 1 (oat1)–mediated transport. Drug Metab. Dispos. *42*, 1357–1366.

Arumugam, T., Ramachandran, V., Fournier, K.F., Wang, H., Marquis, L., Abbruzzese, J.L., Gallick, G.E., Logsdon, C.D., McConkey, D.J., and Choi, W. (2009). Epithelial to mesenchymal transition contributes to drug resistance in pancreatic cancer. Cancer Res. *69*, 5820–5828.

Balakrishnan, A., Goodpaster, T., Randolph-Habecker, J., Hoffstrom, B.G., Jalikis, F.G., Koch, L.K., Berger, C., Kosasih, P.L., Rajan, A., and Sommermeyer, D. (2017). Analysis of ROR1 protein expression in human cancer and normal tissues. Clin. Cancer Res. *23*, 3061–3071.

Bansal, A., and Simon, M.C. (2018). Glutathione metabolism in cancer progression and treatment resistance. J. Cell Biol. *217*, 2291–2298.

Bott, A.J., Shen, J., Tonelli, C., Zhan, L., Sivaram, N., Jiang, Y.-P., Yu, X., Bhatt, V., Chiles, E., and Zhong, H. (2019). Glutamine anabolism plays a critical role in pancreatic cancer by coupling carbon and nitrogen metabolism. Cell Rep. *29*, 1287–1298.e6.

César-Razquin, A., Snijder, B., Frappier-Brinton, T., Isserlin, R., Gyimesi, G., Bai, X., Reithmeier, R.A., Hepworth, D., Hediger, M.A., and Edwards, A.M. (2015). A call for systematic research on solute carriers. Cell *162*, 478–487.

Chong, J., Soufan, O., Li, C., Caraus, I., Li, S., Bourque, G., Wishart, D.S., and Xia, J. (2018). MetaboAnalyst 4.0: towards more transparent and integrative metabolomics analysis. Nucleic Acids Res. *46*, W486–W494.

Corcoran, R.B., Contino, G., Deshpande, V., Tzatsos, A., Conrad, C., Benes, C.H., Levy, D.E., Settleman, J., Engelman, J.A., and Bardeesy, N. (2011). STAT3 plays a critical role in KRAS-induced pancreatic tumorigenesis. Cancer Res. *71*, 5020–5029.

Cui, B., Ghia, E.M., Chen, L., Rassenti, L.Z., DeBoever, C., Widhopf, G.F., Yu, J., Neuberg, D.S., Wierda, W.G., and Rai, K.R. (2016). High-level ROR1 associates with accelerated disease progression in chronic lymphocytic leukemia. Blood *128*, 2931–2940.

Cui, B., Zhang, S., Chen, L., Yu, J., Widhopf, G.F., Fecteau, J.-F., Rassenti, L.Z., and Kipps, T.J. (2013). Targeting ROR1 inhibits epithelial–mesenchymal transition and metastasis. Cancer Res. *73*, 3649–3660.

D'Amico, S., Shi, J., Martin, B.L., Crawford, H.C., Petrenko, O., and Reich, N.C. (2018). STAT3 is a master regulator of epithelial identity and KRAS-driven tumorigenesis. Genes Dev. *32*, 1175–1187.

Daneshmanesh, A., Hojjat-Farsangi, M., Khan, A., Jeddi-Tehrani, M., Akhondi, M., Bayat, A., Ghods, R., Mahmoudi, A., Hadavi, R., and Österborg, A. (2012). Monoclonal antibodies against ROR1 induce apoptosis of chronic lymphocytic leukemia (CLL) cells. Leukemia *26*, 1348–1355.

Duan, P., and You, G. (2009). Novobiocin is a potent inhibitor for human organic anion transporters. Drug Metab. Dispos. *37*, 1203–1210.

Edsbäcker, E., Serviss, J.T., Kolosenko, I., Palm-Apergi, C., De Milito, A., and Tamm, K.P. (2019). STAT3 is activated in multicellular spheroids of colon carcinoma cells and mediates expression of IRF9 and interferon stimulated genes. Sci. Rep. *9*, 536.

El-Gebali, S., Bentz, S., Hediger, M.A., and Anderle, P. (2013). Solute carriers (SLCs) in cancer. Mol. Aspects Med. *34*, 719–734.

Elia, I., Broekaert, D., Christen, S., Boon, R., Radaelli, E., Orth, M.F., Verfaillie, C., Grünewald, T.G., and Fendt, S.-M. (2017). Proline metabolism supports metastasis formation and could be inhibited to selectively target metastasizing cancer cells. Nat. Commun. *8*, 1–11.

Elia, I., Doglioni, G., and Fendt, S.-M. (2018). Metabolic hallmarks of metastasis formation. Trends Cell Biol. *28*, 673–684.

Estrela, J.M., Ortega, A., Mena, S., Sirerol, J.A., and Obrador, E. (2016). Glutathione in metastases: from mechanisms to clinical applications. Crit. Rev. Clin. Lab. Sci. *53*, 253–267.

Fang, X., Liu, Y., Xiao, W., Zhao, N., Zhu, C., Yu, D., and Zhao, Y. (2021). Prognostic SLC family genes promote cell proliferation, migration, and invasion in hepatocellular carcinoma. Acta Biochim. Biophys. Sin. *53*, 1065–1075.

Ferrajoli, A., Faderl, S., Van, Q., Koch, P., Harris, D., Liu, Z., Hazan-Halevy, I., Wang, Y., Kantarjian, H.M., and Priebe, W. (2007). WP1066 disrupts Janus kinase-2 and induces caspase-dependent apoptosis in acute myelogenous leukemia cells. Cancer Res. *67*, 11291–11299.

Fong, M.Y., Zhou, W., Liu, L., Alontaga, A.Y., Chandra, M., Ashby, J., Chow, A., O'Connor, S.T.F., Li, S., and Chin, A.R. (2015). Breast-cancer-secreted miR-122 reprograms glucose metabolism in premetastatic niche to promote metastasis. Nat. Cell. Biol. *17*, 183–194.

Garibsingh, R.-A.A., and Schlessinger, A. (2019). Advances and challenges in rational drug design for SLCs. Trends Pharmacol. Sci. *40*, 790–800.

Hanada, T., Kobayashi, T., Chinen, T., Saeki, K., Takaki, H., Koga, K., Minoda, Y., Sanada, T., Yoshioka, T., and Mimata, H. (2006). IFNγ-dependent, spontaneous development of colorectal carcinomas in SOCS1-deficient mice. J. Exp. Med. *203*, 1391–1397.

Harris, I.S., Treloar, A.E., Inoue, S., Sasaki, M., Gorrini, C., Lee, K.C., Yung, K.Y., Brenner, D., Knobbe-Thomsen, C.B., and Cox, M.A. (2015). Glutathione and thioredoxin antioxidant pathways synergize to drive cancer initiation and progression. Cancer Cell *27*, 211–222.

Haug, K., Cochrane, K., Nainala, V.C., Williams, M., Chang, J., Jayaseelan, K.V., and O'Donovan, C. (2020). MetaboLights: a resource evolving in response to the needs of its scientific community. Nucleic Acids Res. *48*, D440–D444.

Höglund, P.J., Nordström, K.J., Schiöth, H.B., and Fredriksson, R. (2011). The solute carrier families have a remarkably long evolutionary history with the majority of the human families present before divergence of Bilaterian species. Mol. Biol. Evol. *28*, 1531–1541.

Hojjat-Farsangi, M., Moshfegh, A., Daneshmanesh, A.H., Khan, A.S., Mikaelsson, E., Österborg, A., and Mellstedt, H. (2014). The receptor tyrosine kinase ROR1–an oncofetal antigen for targeted cancer therapy. In Seminars in cancer biology (Elsevier), pp. 21–31.

Hu, T., Shukla, S.K., Vernucci, E., He, C., Wang, D., King, R.J., Jha, K., Siddhanta, K., Mullen, N.J., and Attri, K.S. (2021). Metabolic rewiring by loss of Sirt5 promotes Kras-induced pancreatic cancer progression. Gastroenterology *161*, 1584–1600.

Imai, D., Yoshizumi, T., Okano, S., Itoh, S., Ikegami, T., Harada, N., Aishima, S., Oda, Y., and Maehara, Y. (2019). IFN-γ promotes epithelial-mesenchymal transition and the expression of PD-L1 in pancreatic cancer. J. Surg. Res. *240*, 115–123.

Jia, M., Qin, D., Zhao, C., Chai, L., Yu, Z., Wang, W., Tong, L., Lv, L., Wang, Y., and Rehwinkel, J. (2020). Redox homeostasis maintained by GPX4 facilitates STING activation. Nat. Immunol. *21*, 727–735.

Jung, Y., Jun, Y., Lee, H.-Y., Kim, S., Jung, Y., Keum, J., Lee, Y.S., Cho, Y.B., Lee, S., and Kim, J. (2015). Characterization of SLC22A18 as a tumor suppressor and novel biomarker in colorectal cancer. Oncotarget *6*, 25368.

Koepsell, H. (2013). The SLC22 family with transporters of organic cations, anions and zwitterions. Mol. Aspects Med. *34*, 413–435.

Lamouille, S., Xu, J., and Derynck, R. (2014). Molecular mechanisms of epithelial–mesenchymal transition. Nat. Rev. Mol. Cell. Biol. *15*, 178.

Li, P., Harris, D., Liu, Z., Liu, J., Keating, M., and Estrov, Z. (2010). Stat3 activates the receptor tyrosine kinase like orphan receptor-1 gene in chronic lymphocytic leukemia cells. PLoS One *5*, e11859.

Liao, Y., Smyth, G.K., and Shi, W. (2019). The R package Rsubread is easier, faster, cheaper and better for alignment and quantification of RNA sequencing reads. Nucleic Acids Res. *47*, e47.

Lin, L., Yee, S.W., Kim, R.B., and Giacomini, K.M. (2015). SLC transporters as therapeutic targets: emerging opportunities. Nat. Rev. Drug Discov. *14*, 543.

Liu, X., Ser, Z., Cluntun, A.A., Mentch, S.J., and Locasale, J.W. (2014). A strategy for sensitive, large scale quantitative metabolomics. J. Vis. Exp. *87*, e51358.

Lollini, P.L., Bosco, M.C., Cavallo, F., De Giovanni, C., Giovarelli, M., Landuzzi, L., Musiani, P., Modesti, A., Nicoletti, G., and Palmieri, G. (1993). Inhibition of tumor growth and enhancement of metastasis after transfection of the γ-interferon gene. Int. J. Cancer *55*, 320–329.

Loo, J.M., Scherl, A., Nguyen, A., Man, F.Y., Weinberg, E., Zeng, Z., Saltz, L., Paty, P.B., and Tavazoie, S.F. (2015). Extracellular metabolic energetics can promote cancer progression. Cell *160*, 393–406.

Minn, A.J. (2015). Interferons and the immunogenic effects of cancer therapy. Trends Immunol. *36*, 725–737.

Mody, H.R., Hung, S.W., Pathak, R.K., Griffin, J., Cruz-Monserrate, Z., and Govindarajan, R. (2017). miR-202 diminishes TGFβ receptors and attenuates TGFβ1-Induced EMT in pancreatic cancer. Mol. Cancer Res. *15*, 1029–1039.

Mojic, M., Takeda, K., and Hayakawa, Y. (2018). The dark side of IFN-γ: its role in promoting cancer immunoevasion. Int. J. Mol. Sci. *19*, 89.

Neoptolemos, J.P., Kleeff, J., Michl, P., Costello, E., Greenhalf, W., and Palmer, D.H. (2018). Therapeutic developments in pancreatic cancer: current and future perspectives. Nat. Rev. Gastroenterol. Hepatol. *15*, 333.

Olive, K.P., Jacobetz, M.A., Davidson, C.J., Gopinathan, A., McIntyre, D., Honess, D., Madhu, B., Goldgraben, M.A., Caldwell, M.E., and Allard, D. (2009). Inhibition of Hedgehog signaling enhances delivery of chemotherapy in a mouse model of pancreatic cancer. Science *324*, 1457–1461.

Panda, S., Banerjee, N., and Chatterjee, S. (2020). Solute carrier proteins and c-Myc: a strong connection in cancer progression. Drug Discov. Today *25*, 891–900.

Parker, S.J., Amendola, C.R., Hollinshead, K.E., Yu, Q., Yamamoto, K., Encarnación-Rosado, J., Rose, R.E., LaRue, M.M., Sohn, A.S., and Biancur, D.E. (2020). Selective alanine transporter utilization creates a targetable metabolic niche in pancreatic cancer. Cancer Discov. *10*, 1018–1037.

Payen, V.L., Hsu, M.Y., Rädecke, K.S., Wyart, E., Vazeille, T., Bouzin, C., Porporato, P.E., and Sonveaux, P. (2017). Monocarboxylate transporter MCT1 promotes tumor metastasis independently of its activity as a lactate transporter. Cancer Res. *77*, 5591–5601.

Pereira, B.A., Vennin, C., Papanicolaou, M., Chambers, C.R., Herrmann, D., Morton, J.P., Cox, T.R., and Timpson, P. (2019). CAF subpopulations: a new reservoir of stromal targets in pancreatic Cancer. Trends Cancer *5*, 724–741.

Piskounova, E., Agathocleous, M., Murphy, M.M., Hu, Z., Huddlestun, S.E., Zhao, Z., Leitch, A.M., Johnson, T.M., DeBerardinis, R.J., and Morrison, S.J. (2015). Oxidative stress inhibits distant metastasis by human melanoma cells. Nature *527*, 186–191.

Provance, O.K., and Lewis-Wambi, J. (2019). Deciphering the role of interferon alpha signaling and microenvironment crosstalk in inflammatory breast cancer. Breast Cancer Res. *21*, 59.

Provenzano, P.P., Cuevas, C., Chang, A.E., Goel, V.K., Von Hoff, D.D., and Hingorani, S.R. (2012). Enzymatic targeting of the stroma ablates physical barriers to treatment of pancreatic ductal adenocarcinoma. Cancer Cell *21*, 418–429.

Qing, Y., and Stark, G.R. (2004). Alternative activation of STAT1 and STAT3 in response to interferon-γ. J. Biol. Chem. *279*, 41679–41685.

Recouvreux, M.V., Moldenhauer, M.R., Galenkamp, K.M., Jung, M., James, B., Zhang, Y., Lowy, A., Bagchi, A., and Commisso, C. (2020). Glutamine depletion regulates Slug to promote EMT and metastasis in pancreatic cancer. J. Exp. Med. *217*, e20200388.

Rhim, A.D., Mirek, E.T., Aiello, N.M., Maitra, A., Bailey, J.M., McAllister, F., Reichert, M., Beatty, G.L., Rustgi, A.K., and Vonderheide, R.H. (2012). EMT and dissemination precede pancreatic tumor formation. Cell *148*, 349–361.

Robinson, M.D., McCarthy, D.J., and Smyth, G.K. (2010). edgeR: a Bioconductor package for differential expression analysis of digital gene expression data. Bioinformatics *26*, 139–140.

Rozovski, U., Harris, D.M., Li, P., Liu, Z., Jain, P., Ferrajoli, A., Burger, J.A., Bose, P., Thompson, P.A., and Jain, N. (2019). STAT3-Induced Wnt5a provides chronic lymphocytic leukemia cells with survival advantage. J. Immunol. *203*, 3078–3085.

Sanchez-Niño, M.D., Zheng-Lin, B., Valino-Rivas, L., Sanz, A.B., Ramos, A.M., Luno, J., Goicoechea, M., and Ortiz, A. (2017). Lesinurad: what the nephrologist should know. Clin. Kidney J. *10*, 679–687.

Schaller, L., and Lauschke, V.M. (2019). The genetic landscape of the human solute carrier (SLC) transporter superfamily. Hum. Genet. *138*, 1359–1377.

Shakya, R., Gonda, T., Quante, M., Salas, M., Kim, S., Brooks, J., Hirsch, S., Davies, J., Cullo, A., and Olive, K. (2013). Hypomethylating therapy in an aggressive stroma-rich model of pancreatic carcinoma. Cancer Res. *73*, 885–896.

Steele, C.W., Karim, S.A., Leach, J.D., Bailey, P., Upstill-Goddard, R., Rishi, L., Foth, M., Bryson, S., McDaid, K., and Wilson, Z. (2016). CXCR2 inhibition profoundly suppresses metastases and augments immunotherapy in pancreatic ductal adenocarcinoma. Cancer Cell *29*, 832–845.

Subramanian, A., Kuehn, H., Gould, J., Tamayo, P., and Mesirov, J.P. (2007). GSEA-P: a desktop application for gene set enrichment analysis. Bioinformatics *23*, 3251–3253.

Sutherland, R., Meeson, A., and Lowes, S. (2020). Solute transporters and malignancy: establishing the role of uptake transporters in breast cancer and breast cancer metastasis. Can. Metas. Rev. *39*, 919–932.

Tagde, A., Singh, H., Kang, M., and Reynolds, C. (2014). The glutathione synthesis inhibitor buthionine sulfoximine synergistically enhanced melphalan activity against preclinical models of multiple myeloma. Blood Cancer J. *4*, e229.

Tan, P.K., Liu, S., Gunic, E., and Miner, J.N. (2017). Discovery and characterization of verinurad, a potent and specific inhibitor of URAT1 for the treatment of hyperuricemia and gout. Sci. Rep. *7*, 1–11.

Tan, P.K., Ostertag, T.M., and Miner, J.N. (2016). Mechanism of high affinity inhibition of the human urate transporter URAT1. Sci. Rep. *6*, 1–13.

Taniguchi, K., Petersson, M., Höglund, P., Kiessling, R., Klein, G., and Kärre, K. (1987). Interferon gamma induces lung colonization by intravenously inoculated B16 melanoma cells in parallel with enhanced expression of class I major histocompatibility complex antigens. Proc. Natl. Acad. Sci. U S A *84*, 3405–3409.

Tao, L., Lemoff, A., Wang, G., Zarek, C., Lowe, A., Yan, N., and Reese, T.A. (2020). Reactive oxygen species oxidize STING and suppress interferon production. ELife *9*, e57837.

Tseng, H.-C., Lyu, P.-C., and Lin, W.-c. (2010). Nuclear localization of orphan receptor protein kinase (Ror1) is mediated through the juxtamembrane domain. BMC Cell Biol. *11*, 48.

Van Geldermalsen, M., Wang, Q., Nagarajah, R., Marshall, A., Thoeng, A., Gao, D., Ritchie, W., Feng, Y., Bailey, C., and Deng, N. (2016). ASCT2/SLC1A5 controls glutamine uptake and tumour growth in triple-negative basal-like breast cancer. Oncogene *35*, 3201–3208.

Velichko, S., Wagner, T.C., Turkson, J., Jove, R., and Croze, E. (2002). STAT3 activation by type I interferons is dependent on specific tyrosines located in the cytoplasmic domain of interferon receptor chain 2c activation OF multiple stats proceeds through the redundant usage OF two tyrosine residues. J. Biol. Chem. *277*, 35635–35641.

Wang, W., and Zou, W. (2020). Amino acids and their transporters in T cell immunity and cancer therapy. Mol. Cell *80*, 384–395.

Weadick, B., Nayak, D., Persaud, A.K., Hung, S.W., Raj, R., Campbell, M.J., Chen, W., Li, J., Williams, T.M., and Govindarajan, R. (2021). EMT-induced gemcitabine resistance in pancreatic cancer involves the functional loss of equilibrative nucleoside transporter 1. Mol. Cancer Ther. *20*, 410–422.

Wörmann, S.M., Song, L., Ai, J., Diakopoulos, K.N., Kurkowski, M.U., Görgülü, K., Ruess, D., Campbell, A., Doglioni, C., and Jodrell, D. (2016). Loss of P53 function activates JAK2–STAT3 signaling to promote pancreatic tumor growth, stroma modification, and gemcitabine resistance in mice and is associated with patient survival. Gastroenterology *151*, 180–193.e12.

Xiao, M., Wang, C., Zhang, J., Li, Z., Zhao, X., and Qin, Z. (2009). IFNγ promotes papilloma development by up-regulating Th17-associated inflammation. Cancer Res. *69*, 2010–2017.

Xiong, Y., Xiao, C., Li, Z., and Yang, X. (2021). Engineering nanomedicine for glutathione depletion-augmented cancer therapy. Chem. Soc. Rev. *50*, 6013–6041.

Yu, G., Wang, L.-G., Han, Y., and He, Q.-Y. (2012). clusterProfiler: an R package for comparing biological themes among gene clusters. OMICS *16*, 284–287.

Zaidi, M.R. (2019). The interferon-gamma paradox in cancer. J. Interferon Cytokine Res. *39*, 30–38.

Zhang, S., Cui, B., Lai, H., Liu, G., Ghia, E.M., Widhopf, G.F., Zhang, Z., Wu, C.C., Chen, L., and Wu, R. (2014). Ovarian cancer stem cells express ROR1, which can be targeted for anti–cancer-stem-cell therapy. Proc. Natl. Acad. Sci. U S A *111*, 17266–17271.

Zheng, X., Carstens, J.L., Kim, J., Scheible, M., Kaye, J., Sugimoto, H., Wu, C.-C., LeBleu, V.S., and Kalluri, R. (2015). Epithelial-to-mesenchymal transition is dispensable for metastasis but induces chemoresistance in pancreatic cancer. Nature *527*, 525–530.

Zhu, G., Qian, M., Lu, L., Chen, Y., Zhang, X., Wu, Q., Liu, Y., Bian, Z., Yang, Y., and Guo, S. (2019). O-GlcNAcylation of YY1 stimulates tumorigenesis in colorectal cancer cells by targeting SLC22A15 and AANAT. Carcinogenesis *40*, 1121–1131.

Zhu, Y., Karakhanova, S., Huang, X., ping Deng, S., Werner, J., and Bazhin, A.V. (2014). Influence of interferon-α on the expression of the cancer stem cell markers in pancreatic carcinoma cells. Exp. Cell Res. *324*, 146–156.

STAR★METHODS

KEY RESOURCES TABLE

REAGENT or RESOURCE	SOURCE	IDENTIFIER
Antibodies		
Rabbit polyclonal anti-SLCO1A2	Abcam	Cat# ab105124; RRID: AB_10712008
Rabbit polyclonal anti-SLC5A4	Sigma-Aldrich	Cat# AV43940; RRID: AB_1857357
Rabbit polyclonal anti-SLC5A12	Abcam	Cat# ab107749; RRID: AB_10864245
Rabbit polyclonal anti-SLC6A1	Sigma-Aldrich	Cat# HPA013341; RRID: AB_1849509
Rabbit polyclonal anti-SLC6A11	Thermo Fisher Scientific	Cat# PA5-45004; RRID: AB_2608709
Rabbit polyclonal anti-SLC6A16	Thermo Fisher Scientific	Cat# PA5-75896; RRID: AB_2719624
Rabbit polyclonal anti-SLC6A16	Abcam	Cat# ab201294
Rabbit polyclonal anti-SLC22A9	Thermo Fisher Scientific	Cat# PA5-70675; RRID: AB_2690603
Rabbit polyclonal anti-SLC22A10	Sigma-Aldrich	Cat# SAB2105529; RRID: AB_10743192
Rabbit polyclonal anti-SLC22A10	Thermo Fisher Scientific	Cat# PA5-69255; RRID: AB_2689102
Rabbit polyclonal anti-SLC22A12	Sigma-Aldrich	Cat# HPA024575; RRID: AB_1858650
Rabbit polyclonal anti-SLC22A15	Sigma-Aldrich	Cat# SAB2105547; RRID: AB_10743471
Rabbit polyclonal anti-SLC22A15	Thermo Fisher Scientific	Cat# PA5-54080; RRID: AB_2647384
Mouse monoclonal anti-E-cadherin	Thermo Fisher Scientific	Cat# 13-1700; RRID: AB_2533003
Mouse monoclonal anti-N-cadherin	BD Biosciences	Cat# 610921; RRID: AB_398236
Rabbit monoclonal anti-ZEB1	Cell Signaling Technology	Cat# 3396; RRID: AB_1904164
Rabbit monoclonal anti-SLUG	Cell Signaling Technology	Cat# 9585; RRID: AB_2239535
Rabbit monoclonal anti-Vimentin	Cell Signaling Technology	Cat# 5741; RRID: AB_10695459
Rabbit monoclonal anti-ZO-1	Cell Signaling Technology	Cat# 8193; RRID: AB_10898025
Rabbit anti-Twist1	Sigma-Aldrich	Cat# T6451; RRID: AB_609890
Mouse monoclonal anti-Keratin 8/18	Cell Signaling Technology	Cat# 4546; RRID: AB_2134843
Rabbit polyclonal anti-Occludin	Thermo Fisher Scientific	Cat# PA5-30230;, RRID: AB_2547704
Mouse monoclonal anti-EpCAM	Cell Signaling Technology	Cat# 2929; RRID: AB_2098657
Rabbit polyclonal anti-Phospho-ROR1 (Tyr786)	Thermo Fisher Scientific	Cat# PA5-64807; RRID: AB_2663132
Rabbit polyclonal anti-ROR1	Cell Signaling Technology	Cat# 4102; RRID: AB_2180136
Rabbit polyclonal anti-ROR1	Thermo Fisher Scientific	Cat# PA5-14726; RRID: AB_2182472
Rabbit monoclonal anti-IFNAR1	Abcam	Cat# ab45172; RRID: AB_775764
Rabbit polyclonal anti-IFNGR1	Abcam	Cat# ab154400
Rabbit monoclonal anti-IRF1	Cell Signaling Technology	Cat# 8478; RRID: AB_10949108
Rabbit monoclonal anti-IRF9	Cell Signaling Technology	Cat# 76684; RRID: AB_2799885
Rabbit monoclonal anti-phospho-STAT3 (Tyr705)	Cell Signaling Technology	Cat# 9145; RRID: AB_2491009
Mouse monoclonal anti-STAT3	Cell Signaling Technology	Cat# 9139; RRID: AB_331757
Goat anti-rabbit IgG-h+l HRP Conjugated	Bethyl Laboratories	Cat# A120-201P; RRID: AB_67265
Goat anti-mouse IgG-h+l HRP Conjugated	Bethyl Laboratories	Cat# A90-116P; RRID: AB_67183
Mouse monoclonal anti-β-actin	Sigma-Aldrich	Cat# A5316; RRID: AB_476743
Bacterial and virus strains		
TOP10 chemically competent *E. coli* cells	Thermo Fisher Scientific	Cat# C404003
NEB 5-alpha F′ I^q competent *E. coli* cells	New England Biolabs	Cat# C2992I
NEB Stable competent *E. coli* cells	New England Biolabs	Cat# C3040I

(*Continued on next page*)

Continued

REAGENT or RESOURCE	SOURCE	IDENTIFIER
GIPZ Lentiviral Empty Vector shRNA Control (glycerol stock)	Dharmacon, Inc.	Cat# RHS4349
SLC22A10 GIPZ Human Lentiviral shRNA Individual Clone # A	Dharmacon, Inc.	Cat# RHS4430-200199019
SLC22A10 GIPZ Human Lentiviral shRNA Individual Clone # B	Dharmacon, Inc.	Cat# RHS4430-200302125
SLC22A10 GIPZ Human Lentiviral shRNA Individual Clone # C	Dharmacon, Inc.	Cat# RHS4430-200302546
SLC22A15 GIPZ Human Lentiviral shRNA Individual Clone # A	Dharmacon, Inc.	Cat# RHS4430-200172226
SLC22A15 GIPZ Human Lentiviral shRNA Individual Clone # B	Dharmacon, Inc.	Cat# RHS4430-200210168
SLC22A15 GIPZ Human Lentiviral shRNA Individual Clone # C	Dharmacon, Inc.	Cat# RHS4430-200231279
ROR1 GIPZ Human Lentiviral shRNA Individual clone	Dharmacon, Inc	Cat# RHS4430-200224719
pHAGE-ROR1	Addgene	Cat# 116789
psPAX2	Addgene	Cat# 12260
pMD2.G	Addgene	Cat# 12259
Biological samples		
Human multi-organ tissue microarray	Biomax (www.biomax.us/)	Cat# BN243c
Human pancreatic cancer tissue microarray	Biomax (www.biomax.us/)	Cat# PA1921a
Chemicals, peptides, and recombinant proteins		
DMEM	Corning	Cat# 10-013-CV
Opti-MEM	Thermo Fisher Scientific	Cat# 31985-070
Stellate Cell Medium	ScienCell Research Laboratories	Cat# 5301
Stellate Cell Growth Supplement	ScienCell Research Laboratories	Cat# 5352
Pancreatic CAF Maintenance Medium	Vitro Biopharma	Cat# PC00B5
DPBS	Corning	Cat# 21-030-CV
Fetal Bovine Serum	Sigma-Aldrich	Cat# F2442
Penicillin Streptomycin Solution	Corning	Cat# 30-002-CI
0.25% Trypsin EDTA	Corning	Cat# 25-053-CI
Dimethyl sulfoxide	Sigma-Aldrich	Cat# D2650
Lipofectamine 3000	Thermo Fisher Scientific	Cat# L3000-008
Thiazolyl Blue Tetrazolium Bromide (MTT)	Sigma-Aldrich	Cat# M5655
Hexadimethrine bromide (Polybrene)	Sigma-Aldrich	Cat# H9268
L-Glutathione reduced (GSH)	Sigma-Aldrich	Cat# G6013
L-Glutathione oxidized (GSSG)	Sigma-Aldrich	Cat# G4376
D-Fructose 1,6-bisphosphate	Sigma-Aldrich	Cat# F6803
Glutaric acid	Sigma-Aldrich	Cat# G3407
Taurine	Sigma-Aldrich	Cat# T0625
L-Ascorbic acid (Vitamin C)	Sigma-Aldrich	Cat# A92902
L-carnitine hydrochloride	Sigma-Aldrich	Cat# C0283
Carbocysteine	Sigma-Aldrich	Cat# C7757
N1-acetylspermidine	Sigma-Aldrich	Cat# 01467

(*Continued on next page*)

Continued

REAGENT or RESOURCE	SOURCE	IDENTIFIER
N-methyl-D-glucamine chloride	Sigma-Aldrich	Cat# M2004
HEPES-buffered saline	Takara Bio	Cat# S0874
Puromycin Dihydrochloride	Sigma-Aldrich	Cat# P7255
Ampicillin, Sodium salt	EMD Chemicals	Cat# 2200
Kanamycin sulfate	Sigma-Aldrich	Cat# 60615
3M Sodium Acetate pH 5.5	Ambion	Cat# AM9740
Protease Inhibitor Tablets	Sigma-Aldrich	Cat# S8820
Phosphatase Inhibitor Cocktail Tablets	Roche	Cat# 04906837001
PMSF	Millipore-Sigma	Cat# 7110
Crystal Violet	Sigma Aldrich	Cat# C0775
Universal Type I Interferon	PBL assay science	Cat# 11200-1
Recombinant Human IFN-γ	R&D systems	Cat# 285-IF-100
L-Buthionine-sulfoximine	Sigma-Aldrich	Cat# B2515
Gemcitabine hydrochloride	ChemieTek	Cat# CT-GEM
STAT3 Inhibitor III, WP1066	Sigma-Aldrich	Cat# 573097
Interferon-α-IFNα-R-Inhibitor	Sigma-Aldrich	Cat# 407325
Lesinurad	Toronto Research Chemicals	Cat# L329700
Probenecid	Sigma-Aldrich	Cat# P8761
Verinurad	ChemScene	Cat# CS-4681
Benzbromarone	Sigma-Aldrich	Cat# B5774
Sulfinpyrazone	Sigma-Aldrich	Cat# S9509
Lesinurad	Sigma-Aldrich	Cat# SML1607
Novobiocin	Sigma-Aldrich	Cat# N1628
Morin	Sigma-Aldrich	Cat# M4008
Luteolin	Sigma-Aldrich	Cat# L9283
Steviol hydrate	Sigma-Aldrich	Cat# H8664
Matrigel Matrix	Corning	Cat# 354234
Albumin Bovine Fraction V, pH 7 (BSA)	Thermo Scientific	Cat# J10857-36
S.O.C. Bacterial outgrowth medium	Thermo Scientific	Cat# 15544-034
Meta-Phosphoric acid	Sigma-Aldrich	Cat# 239275
Triethanolamine	Sigma-Aldrich	Cat# T58300
[Glycine-2-^{3}H]- Glutathione	American Radiolabeled Chemicals	Cat# ART1180
[3,4-^{3}H]-L-Glutamic acid	Moravek Biochemicals	Cat# MT855
p-[glycyl-2-^{3}H]-Aminohippuric acid	PerkinElmer	Cat# NET053001MC
ULTIMA GOLD liquid scintillation cocktail	PerkinElmer	Cat# 6013329
Tween-80	Sigma-Aldrich	Cat# P1754
Critical commercial assays		
TaqMan® Low Density Arrays (RealTime PCR Systems)	Thermo Fisher Scientific	Production number# 000003081333
BCA Protein assay kit	Thermo Scientific	Cat# 23227
Chemiluminescence Substrate kit	Thermo Scientific	Cat# 34580
E.Z.N.A. Total RNA kit I	OMEGA bio-tek	Cat# R6834-02
E.Z.N.A. Plasmid DNA kit	OMEGA bio-tek	Cat# D6904-04
Glutathione assay kit	Cayman Chemical	Cat# 703002
Human Interferon alpha 1 ELISA kit	Abcam	Cat# ab213479

(*Continued on next page*)

Continued

REAGENT or RESOURCE	SOURCE	IDENTIFIER
Human IFN gamma ELISA kit	Abcam	Cat# ab174443
Deposited data		
Human RNA-seq data	Gene Expression Omnibus Repository	GEO: GSE155909
Untargeted metabolomics data	EMBL-EBI MetaboLights database	MetaboLights: MTBLS1925
Experimental models: Cell lines		
Human: PANC-1 cells	ATCC	Cat# CRL-1469
Human: HPAF-II cells	ATCC	Cat# CRL-1997
Human: HEK 293T/17 cells	ATCC	Cat# CRL-11268
Human: Isogenic epithelial clones (Epi)	Isolated in-house	N/A
Human: Isogenic mesenchymal clones (Mes)	Isolated in-house	N/A
Pancreatic stellate cells (PSCs)	ScienCell Research Laboratories	Cat# 3830
Pancreatic cancer-associated fibroblasts (PCAFs)	Vitro Biopharma	Cat# CAF08
Experimental models: Organisms/strains		
Mouse: KPC (LSL-KrasG12D/+; LSL-Trp53R270H/+; Pdx-1-Cre)	Target Validation Shared Resources, OSUCCC	Strain: # 129/B6/FVB
Mouse: homozygous nude (Foxn1^{nu}/Foxn1^{nu})	The Jackson Laboratory	Cat# 007850
Oligonucleotides		
Primers information for qRT-PCR: assay IDs provided in Table S1	This paper	N/A
Recombinant DNA		
pLenti-III-Blank vector	Applied Biological Material Inc.	Cat# LV587
pLV-puro-SLCO1A2-Myc	Sino Biological Inc.	Cat# HG18927-CMLP
pLV-puro-SLC5A4-Myc	Sino Biological Inc.	Cat# HG20938-CMLP
pLV-puro-SLC5A12-Myc	Sino Biological Inc.	Cat# HG26093-CMLP
pLV-puro-SLC6A1-Myc	Sino Biological Inc.	Cat# HG13111-CMLP
pLV-puro-SLC6A11-Myc	Sino Biological Inc.	Cat# HG21690-CMLP
pLV-puro-SLC6A16-Myc	Sino Biological Inc.	Cat# HG25125-CMLP
pLV-puro-SLC22A9-Myc	Sino Biological Inc.	Cat# HG21277-CMLP
pLV-puro-SLC22A10-t1-Myc	Sino Biological Inc.	Cat# HG25463-CMLP
pLV-puro-SLC22A12-Myc	Sino Biological Inc.	Cat# HG18213-CMLP
pLV-puro-SLC22A15-Myc	Sino Biological Inc.	Cat# HG25739-CMLP
Software and algorithms		
GraphPad Prism 7.04	GraphPad Inc.	http://graphpad.com
ImageJ Fiji (version 2.0.0-rc44)	N/A	https://fiji.sc/
SoftMax Pro	Molecular Devices	https://www.moleculardevices.com/
Rsubread	Bioconductor	http://bioconductor.org. PMID:30783653
edgeR	Bioconductor	http://bioconductor.org. PMID: 19910308
GSEA	Broad Institute	http://software.broadinstitute.org/gsea/index.jsp/. PMID: 16199517
MetaboAnalyst	N/A	https://www.metaboanalyst.ca/
ITK-SNAP 3.8.0	N/A	http://www.itksnap.org/
ChemDraw Professional 17.1	PerkinElmer	https://www.perkinelmer.com/
SAS 9.4	The SAS Institute, Cary, NC	https://www.sas.com/

(*Continued on next page*)

Continued

REAGENT or RESOURCE	SOURCE	IDENTIFIER
Others		
Biocoat Matrigel Invasion Chamber	Corning	Cat# 354480
Transwell Permeable Supports	Corning	Cat# 3422
PVDF membrane for protein blotting	BIORAD	Cat# 1620177
MONOCRYL sterile absorbable suture	ETHICON	Cat# Y426H
X-tremeGENE HP DNA transfection reagent	Roche	Cat# 06366236001

RESOURCE AVAILABILITY

Lead contact

Correspondence and requests for materials should be addressed to R. Govindarajan (govindarajan.21@osu.edu).

Material availability

The study did not generate any unique materials.

Data and code availability

RNA sequencing data of pLV-Control, pLV-SLC22A10_OE, and pLV-SLC22A15_OE clones can be found at the Gene Expression Omnibus Repository (GEO) accession number GSE155909. Metabolomics data have been deposited to the EMBL-EBI MetaboLights database (Haug et al., 2020) with the identifier MetaboLights: MTBLS1925. All software packages used are publicly available upon request or through commercial vendors. Any additional information required to reanalyze the data reported in this paper is available from the lead contact upon request.

EXPERIMENTAL MODEL AND SUBJECT DETAILS

Mouse models and ethics statement

Eight-week-old female athymic nude mice (homozygous for Foxn1<nu>) were procured from The Jackson Laboratory (stock no. 007850). KPC mice were bred by the Target Validation Shared Resource (TVSR) at the Ohio State University Comprehensive Cancer Center (OSUCCC). The following mouse strains were acquired from the National Cancer Institute Frederick Mouse Repository for interbreeding to generate KPC mice: *Kras*$^{LSL\text{-}G12D}$ (strain number 01XJ6), *p53*$^{LSL\text{-}R270H}$ (strain number 01XM3) and *Pdx1-cre* (strain number 01XL5). The KPC mice used in this study were maintained on a mixed 129/B6/FVB strain background (Shakya et al., 2013). Slc22a15 floxed mice were generated at the Genetically Engineered Mouse Modeling Core (GEMMC) of the Ohio State University Comprehensive Cancer Center (OSUCCC). B6.FVB-Tg (EIIa-cre) C5379Lmgd/J CRE line was obtained from The Jackson Laboratory (stock no: 003724). The animals were housed under pathogen-free conditions in microisolator cages with food and water available *ad libitum*. Animal experiments were performed in accordance with our protocol (2015A00000095-R1), which was approved by the Institutional Animal Care and Use Committee (IACUC) at The Ohio State University (Columbus, OH).

Normal human tissue samples and human pancreatic tumor microarray

Pancreatic cancer TMA consisting of 96 human pancreatic ductal adenocarcinoma specimens were obtained from US Biomax, Inc. (Catalog no. PA1921a) (Table S2). To optimize immunohistochemical expression analyses of SLC22A10 and SLC22A15 in human tissues, multi-organ tissue microarray slides were procured from US BioMax Inc. (Catalog no. BN243c), which included normal human pancreas, brain, cardiac muscle, lung, liver, cervix, colon, kidney, breast, ovary, prostate, and skin tissues.

Cell lines and culture conditions

Human PDAC cells (PANC-1, MiaPaca-2, Capan-1, AsPC-1, and HPAF-II) and HEK 293T/17 (lentiviral packaging cells) cells were obtained from American Type Culture Collection (ATCC), Manassas, VA. ATCC uses morphological, cytogenetic, and DNA profiling for the characterization of the cell lines. Human pancreatic ductal epithelial (HPDE) cells were kindly provided by Dr. Ming Tsao, Ontario Cancer Institute and the

L3.6PL cell line was a kind gift from Dr. Isiah D. Fidler at The University of Texas MD Anderson Cancer Center. Isogenic E-cadherin-enriched Epi and N-cadherin-enriched Mes clones were isolated and characterized from PANC-1 cells as described earlier (Weadick et al., 2021). Mouse pancreatic tumor cells derived from a *PDX-1-CRE*, *LSL-KRas*^{G12D}, LSL-Trp53$^{-/-}$ (KPC) genetically engineered mouse model of pancreatic cancer were described earlier (Mody et al., 2017; Olive et al., 2009). The PANC-1, MiaPaca-2, HEK293T/17 cell lines and Epi and Mes clones were cultured using Dulbecco's modified Eagle medium (DMEM) supplemented with 10% fetal bovine serum (FBS) and 1× penicillin-streptomycin antibiotics. Capan-1 cells were cultured in Iscove's Modified Dulbecco's Medium supplemented with 20% FBS, AsPC-1 cells in RPMI-1640 supplemented with 10% FBS, and HPAF-II cells were cultured in Eagle's Minimum Essential Medium (MEM) supplemented with 10% FBS. L3.6PL cells were cultured in MEM supplemented with 10% FBS, 1% non-essential amino acid solution 100× (Gibco), 1% 100 mM sodium pyruvate (Gibco), 1% 200 mM L-glutamine (Gibco), and 2% 100× vitamins (Gibco). HPDE cells were cultured in Keratinocyte serum free medium supplemented with human recombinant epidermal growth factor and bovine pituitary extract (Gibco). Human pancreatic stellate cells (PSCs) were procured from ScienCell Research laboratories (3830) and cultured in Stellate Cell Medium (SteCM) with added Stellate Cell Growth Supplement (SteCGS) (ScienCell), 2% FBS, and above antibiotics. Human pancreatic cancer-associated fibroblasts (PCAFs) were obtained from Vitro Biopharma (CAF08) and grown in pancreatic CAF maintenance medium. All the above cell lines were received as frozen stocks and were propagated, expanded, and frozen after their arrival. Cell subculture was performed every 2–3 days to maintain a healthy growth rate, and cells were periodically tested for mycoplasma contamination using the MycoProbe Mycoplasma Detection Kit (R&D Systems CUL001B). Cells within 10–20 passages were used for performing the experiments. For the conditioned medium preparation, fresh culture medium was added to PSCs and PCAFs at >70% confluency. The medium was harvested after 24 h and passed through 0.45-μm syringe filters.

METHOD DETAILS

Lentiviral transduction and generation of stable cell lines

Cells were transfected using X-tremeGENE HP DNA transfection reagent (Roche 6366546001) following the manufacturer's protocol. Lentiviral production was carried out by cotransfection of 293T cells with the lentiviral expression plasmids or shRNAs with the lentiviral envelope pMD2.G (Addgene 12259) and packaging plasmids psPAX2 (Addgene 12260) in a 4:1.5:2 ratio. Supernatant containing the virus was harvested 36 and 60 h after transfection, pooled, filtered through a 0.45-μm filter, layered with 10 μg/mL polybrene, and transduced to the target cells twice with an interval of 24 h. The infected cells were then allowed to recover for 24 h, and polyclonal clones with stable gene expression were selected for with puromycin.

RNA-seq, differential expression analysis and gene set enrichment analysis

Strand-specific RNA-seq libraries were prepared using the NEBNext Ultra II Directional RNA Library Prep Kit for Illumina following the manufacturer's recommendations. In summary, total RNA quality was assessed using an RNA 6000 Nano kit on an Agilent 2100 Bioanalyzer (Agilent Biotechnologies), and the concentration was measured using a Qubit RNA HS assay kit (Life Technologies). A 500-ng aliquot of total RNA was depleted of rRNA using a Human/Mouse/Rat RNAse-H based Depletion kit from NEB (New England Biolabs). Following rRNA removal, mRNA was fragmented and then used for first- and second-strand cDNA synthesis with random hexamer primers. Double-stranded cDNA fragments underwent end repair, poly (A) tailing and the ligation of two unique adapters (Integrated DNA Technologies, Coralville, IA). The adaptor-ligated cDNA was amplified by limited-cycle PCR. Library quality was analyzed with TapeStation High-Sensitivity D1000 ScreenTape (Agilent Biotechnologies) and quantified by KAPA qPCR (KAPA BioSystems). Libraries were pooled and sequenced at 2 × 150-bp read lengths on the Illumina HiSeq 4000 platform.

On average, 63 million 151-bp paired-end RNA-seq reads were generated for each sample (the range was 57 million to 70 million). Paired-end sequence reads were aligned to the human genome (hg38) using Rsubread (Liao et al., 2019) (>90% of ~25×10^6 unique reads/sample mapped) and translated to expression counts via featureCounts, followed by analysis via the standard edgeR pipeline (Robinson et al., 2010) to DEGs, visualization with Volcano plots (ggplot2) and interpretation by GSEAs (Subramanian et al., 2007); in particular, enrichment of a hallmarks gene set was analyzed using GSEA. Visualization of enrichment was undertaken with clusterProfiler (Yu et al., 2012), and patterns of differential gene expression were illustrated with Volcano plots and heatmaps.

Unbiased metabolomic profiling and analysis

Samples were prepared based on the methods of Liu et al. (2014). Briefly, vector-transduced and SLC22A10- and SLC22A15-OE clones were seeded at 1 × 10^6 cells per 60-mm cell culture dish (n = 5) and grown to 80% confluence. The cells were replenished with fresh culture media 12 h prior to metabolite extraction. Subsequently, the growth media was aspirated, the plates were placed on dry ice, 2 mL of pre-chilled 80% methanol (−80°C) was added to the cells, and the plates were kept at −80°C for 15 min. Cells and extraction solvent were then harvested using a cell scraper, collected in 2-mL Eppendorf tubes, and centrifuged at 20,000 × g at 4°C for 10 min. Solvent in the supernatant was evaporated in a speed vacuum concentrator at room temperature. Dried metabolites were reconstituted in 100 μL of water containing 0.1% formic acid and centrifuged at 20,000 × g for 10 min at 4°C. Cleared samples were filled into glass autosampler vials for Q-TOF LC-MS/MS analyses. LC-MS/MS analyses were performed on an Agilent 6545 Q-TOF (Santa Clara, CA) in positive ion mode with a dual AJS ESI system and an Agilent 1290 Infinity LC system. Five microliters of each sample were separated on a Kinetex PS C18 column (2.6 μm, 100 Å, 100 × 2.1 mm, Phenomenex). The mobile phase used for the chromatographic separation consisted of solvent A (0.1% formic acid in water) and solvent B (0.1% formic acid in acetonitrile), and the flow rate was 200 μL/min. The chromatographic gradient conditions were optimized as follows: 0–3 min of 2% B, 11.5 min of 45% B, 13 min of 90% B, 20 min of 90% B, 25 min of 2% B, and 30 min of 2% B. Data were acquired in positive electrospray ionization mode. The mass range was set to 50 to 1,700 m/z. The ion source parameters and the mass spectrometry operating conditions were as follows: gas temperature, 250°C; source gas flow, 8 L/min; nebulizer, 25 psi; sheath gas temperature, 350°C; sheath gas flow, 10 L/min; capillary voltage, 3,500 V (positive ion mode); and nozzle voltage, 500 V (positive ion mode). Features were selected using data-dependent acquisition, in which the top 5 ions at a given time point were retained, used to generate a mass spectral profile, and then excluded for a 30-s window. Features were identified using Scaffold Elements v2.1.1. Significant features after familywise error rate (FWER) correction were retained for downstream analyses. Features were identified by searching against the METLIN Metabolite and Chemical Entity Database, NIST database, and Human Metabolite Database (HMDB) metabolite library. Data were filtered based on an ID-score >= 0.8 and a log10 intensity >= 6. Tentatively identified metabolites were imported into MetaboAnalyst (Chong et al., 2018).

[^{3}H] radionuclide transport assay

Cells were seeded in 24-well plates at a density of 1 × 10^5 cells per well and incubated for 24 h. Uptake of radiolabeled substrates: [Glycine-2-^{3}H]-glutathione (American Radiolabeled Chemicals ART1180), p-[glycyl-2-^{3}H]-aminohippuric acid (PerkinElmer NET053001MC), [3,4-^{3}H]-L-glutamic acid (Moravek Biochemicals MT855), (0.02 μM each supplemented in combination with unlabeled substrates to a final concentration of 1 μM) was measured after 20 min of incubation of cell monolayer in presence of Na^+-containing transport buffer (20 mM Tris-HCl, 3 mM dipotassium phosphate, 1 mM magnesium chloride hexahydrate, 2 mM calcium chloride, 5 mM glucose, 130 mM NaCl; pH 7.4) at 37°C. For determining the transport of [Glycine-2-^{3}H]-glutathione in presence of various buffers and pH conditions, the above Na^+-containing buffer at pH 7.4, Na^+-containing buffer at pH 5.5, Na^+-free (NMDG) buffer (20 mM Tris-HCl, 3 mM dipotassium phosphate, 1 mM magnesium chloride hexahydrate, 2 mM calcium chloride, 5 mM glucose, 130 mM N-methyl-D-glucamine chloride (NMDG)), and HBS (HEPES buffered saline) (Takara Bio S0874) were used. At the end of the transport period, the transport buffer was aspirated, and cells were washed with ice-cold wash buffer (contains (100 μM of unlabeled substrate) to arrest the transport process. The cells were then lysed with 10% sodium dodecyl sulfate, and cell lysates were collected into scintillation vials and mixed with ULTIMA GOLD liquid scintillation cocktail (PerkinElmer 6013329) by vigorous vortexing. The radioactivity of each sample in three independent biological replicates was counted using a Beckman LS6500 liquid scintillation counter, and the obtained disintegrations per minute (DPM) values were converted to picomoles based on the specific activity of radionuclides.

Glutathione measurements

30 mg of primary tumor tissues isolated from animals bearing vector-transduced and SLC22A10 OE- and SLC22A15-OE clones were ultrasonicated in ice-cold MES buffer (0.4 M 2-(N-morpholino) ethanesulphonic acid, 0.1 M phosphate, and 2 mM EDTA, pH 6.0), centrifuged, and supernatants were collected. For PSCs and PCAFs, 1 × 10^6 cells from each were cultured in 60 mm Petri dishes for 24 h, harvested in ice-cold MES buffer using cell scrapper, ultrasonicated, centrifuged and supernatants were collected. Samples to quantify total GSH and oxidized GSSG were prepared as described in Glutathione Assay Kit (Cayman Chemical 703002) following the manufacturer's protocol. The GSH and GSSG concentrations in each sample were

estimated using a standard curve and normalized to the quantity of initially processed tissues or protein concentration.

Quantification of IFN-α and IFN-γ by ELISA

Briefly, cells were seeded at a density of 1 × 10^5 cells per well in 12 well plates and incubated for 48 h. Culture plates with cells were then equilibrated to room temperature and conditioned medium (CM) was harvested and filtered using sterile 0.45 μm syringe filter. 50 μL of the CM from each sample was assayed in triplicates and IFN-α and IFN-γ concentrations were determined by ELISA using commercial kits (ab213479 Human Interferon alpha 1 ELISA kit and ab174443 Human IFN gamma ELISA kit) purchased from Abcam following the manufacturer's protocol. Corresponding recombinant proteins at specified concentrations were taken during each test to prepare the standard curves. Absorbance of the standards and samples were measured at 450 nm using a spectrophotometer and concentrations of IFN-α and IFN-γ in the test samples were estimated by comparing the absorbance values with the absorbance of the standard proteins.

Real-time qPCR

Cells were cultured in 60-mm cell culture dishes at a density of 1 × 10^6 cells in growth medium for 24 h. The cells were then lysed, and total RNA was isolated using the E.Z.N.A Total RNA kit I (OMEGA Bio-tek R6834-02) following the manufacturer's protocol. Quantitative real-time PCR was conducted using custom-designed TaqMan Array microfluidic cards (Thermo Fisher Scientific 000003081333) for SLC superfamily of transporters (Table S1). 18S ribosomal RNA was used as a housekeeping gene. The obtained cycle threshold (CT) values were normalized with the housekeeping gene and 2–ΔΔCt method was used to calculate fold changes in mRNA expression, after which a heat map was prepared, and cluster analysis was performed utilizing edgeR software.

Western blotting

Cells were seeded at a density of 1 ×10^6 per dish in 60 mm Petri dishes and incubated for 24 h. Whole-cell lysates were prepared in ice-cold lysis buffer (150 mM NaCl, 1% Triton X-100, 0.1% sodium dodecyl sulfate, 50 mM Tris HCl (pH 8.0), 1 mM EDTA, 2 mM PMSF, 1 mM NaF, protease inhibitor (Sigma-Aldrich S8820) and 1× phosphatase inhibitor (Roche 04906837001)). The protein concentration was determined using a BCA protein assay kit (Thermo Scientific 23227). Following electrophoretic separation by denaturing SDS-PAGE, proteins were transferred onto PVDF membranes (Bio-Rad), and membranes were then blocked overnight in 5% bovine serum albumin (BSA) (Thermo Scientific J10857-36). Subsequently, the membranes were probed with primary antibodies at a 1:1000 dilution in 5% BSA for 3 h at room temperature. After washing thrice with TBST buffer, the blots were further incubated with species-specific HRP-conjugated secondary antibodies at a 1:2000 dilution in 5% skim milk for 1 h. The blots were successively washed another 3 times with TBST, and bands were visualized by the addition of chemiluminescence substrate (Thermo Scientific 34580) and imaging with a ChemiDoc™ Touch Imaging System (Bio-Rad).

Immunocytochemistry

Immunocytochemistry experiments were performed following the standardized procedure by Weadick et al. (2021) with minor modifications. Cells were seeded on coverslips in six-well plates at a density of 0.5 × 10^6 cells per well and incubated for 24 h. Culture medium was aspirated out and cells were then fixed with 2% paraformaldehyde for 15 min; blocked with 5% goat serum in PBST for 1 h and then incubated with primary antibody SLC22A15 (Thermo Fisher Scientific PA5-54080) at 1:250 dilution in solution (1% BSA in PBST) for overnight at 4°C. Cells were gently washed for six times (5 min each wash) and incubated with secondary antibody Alexa Fluor 594 goat anti-rabbit IgG (Invitrogen) at 1:2000 dilution in solution (1% BSA in PBST) for 1 h at room temperature. After subsequent six washes with PBST, cells were counterstained with DAPI staining solution (1 μg/mL) for 5 min and rinsed once with distilled water. Coverslips with cells were then mounted with ProLong Gold antifade mountant (Invitrogen), sealed on a glass slide, visualized and images were captured under a fluorescent microscope (NIKON).

Transwell cell migration and invasion assays

For the migration assay, tissue culture-treated Transwell permeable supports with polycarbonate membrane inserts (Corning 3422), and for the invasion assay, BioCoat cell culture inserts with polyethylene terephthalate (PET) membranes precoated with extracellular matrix proteins (Corning 354480) in a 24-well

format with pore size of 8 μm were used. Briefly, inserts were hydrated by the addition of 20 μL of serum-free DMEM onto the matrix layer, and 600 μL of complete growth medium containing 10% FBS was added to the lower chamber of the plates as a chemoattractant; the plates were then placed inside an incubator for 2 h. Moderately confluent cells in the Petri dishes were trypsinized, and 1 × 10^5 cells in 200 μL of serum-free DMEM were seeded into each well of the upper inserts. The plates were then incubated at 37°C and 5% CO_2 for 48 h. At the end of the incubation period, the media and the noninvading/nonmigrating cells were removed by gently scrubbing the upper surface of the Transwell with a cotton-tipped applicator. The invaded/migrated cells on the lower surface of the membrane were fixed with ice-cold methanol, dried, and stained with 0.2% crystal violet. Cells attached to the underside of the membrane were viewed from underneath with an inverted microscope, and the cells from at least three random fields were counted and photographed at 10× magnification.

Pharmacological inhibitors and formulation preparation

For *in vitro* studies, novobiocin and BSO were dissolved in sterile DPBS, and all other inhibitors were dissolved in cell culture-grade DMSO. Stock solutions of each inhibitor (10 mM) were prepared using the appropriate solvent, aliquoted and stored at −20°C. For cell treatments, individual aliquots were thawed, mixed homogeneously with the culture medium to obtain the desired concentrations, and gently added to the culture dishes. The final concentration for DMSO in each treatment condition was below 0.2%. For *in vivo* studies, drug formulations were freshly prepared each time before their injection into animals. Sterile normal saline (0.9% NaCl) was used as a vehicle for each prepared formulation. To prepare formulations of lesinurad and gemcitabine + lesinurad in combination, the appropriate quantity of lesinurad was first dissolved in 50 μL of DMSO, which was then added to 50 μL of Tween 80 (solubilizer). This mixture was slowly solubilized with either saline or a gemcitabine solution to the required final volume with sonication.

Orthotopic pancreatic tumor xenograft model

Eight-week-old female athymic nude mice were procured from The Jackson Laboratory. Upon arrival, the animals were allowed to acclimatize to their new environment for one week and maintained under pathogen-free conditions. Animals were then randomly caged into groups of 5. Vector-transduced PANC-1 clones, PANC-1 clones stably overexpressing SLCs (*O1A2, 5A4, 5A12, 6A1, 6A11, 6A16, 22A9, 22A10, 22A12, and 22A15*), and Mes clones with stable shRNA transduction (scramble/shRNA control, *shSLC22A10* and *shSLC22A15)* were grown to 80% confluency in 90-mm Petri dishes. On the days of tumor cell implantation, clones were harvested, and individual cell suspension aliquots were prepared by mixing 2 × 10^5 cells in 50 μL of ice-cold Matrigel: PBS (1:1) and kept on ice. Three hours before surgery mice were injected subcutaneously with sustained release analgesia Buprenorphine-SR (1 mg/kg). Animals were then anesthetized using 1%–2% isoflurane, the left side of the abdomen was surgically opened with a 1-cm incision under aseptic conditions, the pancreas was retracted up, and the cells were orthotopically injected into the tail region of the pancreas. The cell suspension was allowed to solidify within the pancreatic tissues for 30 s to avoid leakage from the pancreas. The pancreas was then placed back inside the peritoneal cavity, and the skin incisions were closed with sterile absorbable surgical sutures (MONOCRYL 4–0 poliglecaprone 25; Ethicon Inc., Y426H) and cleaned with povidone-iodine antiseptic solution. Mice were injected with 200 μL of 0.5 mg/mL meloxicam subcutaneously in every 24 h for subsequent three days for the postsurgical pain management. The animals were monitored for changes in body weight twice a week. At the end of the 12^{th} week, the animals were euthanized, necropsied and tumor weights were recorded. Additionally, the liver, spleen, kidneys, intestine, and peritoneal cavity were examined for metastatic foci/lesions. Moreover, tissue sections from the excised tumors were preserved at −80°C for further analysis. For treatments, two weeks after the tumor cell implantation, randomly segregated groups of mice were administered intraperitoneally with saline, gemcitabine (25 mg/kg), lesinurad (25 mg/kg), or combination of gemcitabine + lesinurad (25 mg/kg each) twice a week for 10 weeks. Mice were then euthanized at the end of 12^{th} week for *ex vivo* analysis.

KPC mice treatment regimens and survival analyses

Six- to seven-week-old KPC animals without any apparent disease symptoms were used for the study. The mice were randomized into cohorts, and drug treatment started at 8 weeks of age. Different groups of animals received normal saline, gemcitabine (25 mg/kg) or a combination of gemcitabine + lesinurad (25 mg/kg each) through intraperitoneal administration twice a week. Tumor burden was monitored twice (T1 and T2) with a six-week interval during the treatment period using μCT (SkyScan 1276) at the Small Animal Imaging Core (SAIC) at the Tzagournis Medical Research Facility (The Ohio State University). Drug

treatment was continued until the animals survived or reached early removal criteria for excessive tumor burden. In the latter case, animals were immediately euthanized. Subsequently, complete necropsy examination of the animals was carried out to evaluate total tumor burden and the incidence of metastasis, and tissue specimens were processed for confirmatory IHC tumor diagnosis.

μCT imaging of KPC animals

Twelve hours before scanning, chow was removed from the cages to allow for gastric emptying and promote lassitude. Immediately prior to imaging, 300 μL of contrast agent (300 mg/mL Iohexol diluted in bacteriostatic saline to 20% (v/v)) was injected intraperitoneally. Subjects under 2% isoflurane were imaged with a Bruker SkyScan 1276 (Bruker microCT) for ~8 min. The system offers a 180° plus cone beam angle option for acquisitions in which beam hardening artifacts are unlikely to be a concern. A source voltage of 60 kV and a source current of 200 μA were applied for 199 ms. A 0.8-degree rotation step was used to generate a 16-bit isotropic dataset with a 40.872-μm voxel size. The 0.5-mm AL filter with two averages was used to give the most realistic density values for most of the abdomen. A time-resolved image (breath gating) was attained postprocessing prior to reconstruction of the image. All projections with significantly more contrast or blur compared to most of the dataset were automatically sorted and discarded as they showed unusable movement. For the final reconstruction, the Feldkamp algorithm, calculations from forward/back projections and a Hamming filter were applied. Regions of interest (ROIs) were traced and identified by comparing their anatomical position and size. The resulting tumor volumes and organ volumes were quantified using ITK-SNAP and proprietary software licensed to Bruker.

Multiplexed immunohistochemistry of TMA

Double immunohistochemical staining was performed for Pan-Cytokeratin and SLC22A10 or SLC22A15, respectively. In brief, paraffin was removed from the TMA samples by baking at 60°C for 1 h, followed by two treatments with xylene for 10 min. Next, the slides were rehydrated in an ethanol gradient of 100% ethanol and 95% ethanol for 5 min each and rinsed in 70% ethanol and water. Tissue sections were fixed in 10% neutral-buffered formalin for 20 min. Initial antigen retrieval was performed by microwaving the slides in antigen retrieval buffer pH 9 (Perkin Elmer) at 100% power for 45 s to bring the buffer to a boil, followed by an additional 15 min at 10% power. The slides were cooled at room temperature for 30 min before blocking for 10 min and incubation with Pan-Cytokeratin primary antibody diluted 1:250 for 30 min at room temperature. Then, secondary antibody conjugated to HRP and TSA were incubated with tissue sections for 10 min, followed by the addition of the Opal 570 fluorophore diluted 1:150. A second microwave treatment was performed as described above to strip any unbound fluorophore with antigen retrieval buffer pH 6 (Perkin Elmer). SLC22A10 (1:200) or SLC22A15 (1:100) primary antibody was applied overnight 4°C followed by labeling with Opal 520 fluorophore diluted 1:100. After a final microwave treatment (pH 6 buffer), spectral DAPI was applied for 2 min, and slides were rinsed with TBST and water. Slides were mounted with fluorescent mounting medium and coverslips were applied. Multiplexed TMA slides were imaged with the Vectra 2.0 multispectral imaging system (Perkin Elmer).

IHC image quantification and analysis

Acquired immunohistochemistry images of PDAC tumor tissues were analyzed with inForm software and segmented based on expression of pan-cytokeratin to differentiate tumor from stromal cells. Positivity for expression of SLC22A10 or SLC22A15 was determined by user-defined threshold values for relative staining intensity. Then, cells were sorted based on fluorescent signal intensity into 4 bins (0+, 1+, 2+, and 3+). An H-score was calculated for each tumor sample using the following formula: (1 × (% cells 1+) +2 × (% cells 2+) +3 × (% cells 3+)). H-score values range from 0 to 300, with 300 as the maximum possible score and highest staining intensity.

For the TMA analysis, demographic and clinical characteristics of patients were analyzed using descriptive statistics. Briefly, continuous variables were summarized as mean/standard deviation (SD) or median/range; categorical data were presented as count (n) and frequency (%). Correlation between H-scores of tumor and stromal expression of SLC22A10 and SLC22A15, were compared using both Student's t test and U rank sum test. All tests were two-sided and p values ≤ 0.05 were regarded as statistically significant. SAS 9.4 (The SAS Institute, Cary, NC) was used for analysis.

QUANTIFICATION AND STATISTICAL ANALYSIS

All statistical analyses were performed using GraphPad Prism software v7.04. Data are presented as mean ± SD or mean ± SEM, unless otherwise stated. For comparison between the groups, ANOVA (Dunnett's test or Tukey's test or Sidak's multiple comparison test) or unpaired Student's t-test (two-tailed) was used. For survival analysis, Log-Rank (Mantel-Cox) test was used, and Fisher's exact test was employed to compare between the groups of KPC animals with metastases. $p < 0.05$ was considered statistically significant in all cases.

No statistical method was used to predetermine the sample size. The mouse experiments described in this study followed randomization as described in STAR Method section. The investigators were not blinded to allocation during experiments and outcome assessment except the micro-CT imaging for tracking tumor growth in KPC mice.